9950-861

SEPTEMBER 1979

PARAMETRIC ANALYSIS REPORT
HIGH TEMPERATURE
SOLAR THERMAL RECEIVER
JPL CONTRACT #955454

(NASA-CR-173129) PARAMETRIC ANALYSIS REPORT: HIGH TEMPERATURE SOLAR THERMAL RECEIVER (Sanders Associates, Inc.) 86 p HC A05/MF A01 CSCL 10A

N83-35524

Unclas
H2/44 42155

SANDERS ASSOCIATES, INC.
ENERGY SYSTEMS CENTER
95 Canal Street, Nashua, New Hampshire 03061

86 pages

SEPTEMBER 1979

PARAMETRIC ANALYSIS REPORT
HIGH TEMPERATURE
SOLAR THERMAL RECEIVER
JPL CONTRACT #955454

SUBMITTED: 14 SEPTEMBER 1979

TABLE OF CONTENTS

	Page
Executive Summary	1
Task 1 - Statement of Work	4
Task 1 - Parametric Analyses	4
Concepts	5
Receiver Pressure Drops	16
Working Fluid Effects on Pressure Drops	19
Brayton Cycle Evaluation	22
Engine Parameters	22
Method of Analysis	23
Results	26
Design Point	35
Aperture Sizing	35
Focal Point Location	41
Power Scaling	41
Flux Distribution	46
Window Heat Load	54A
Window Size Limits	62
Instructions for Nomogram Use	64
Material Selection	65
Material Properties	65
Silicon Carbide	66
Cordierite	67
Matrix Receiver	69
Tube and Extended Surface Receivers	71
Availability and Cost	73
Thermal Stresses	76
Weight Estimate	79
Regimes of Operation	80
Recommendations	82

LIST OF ILLUSTRATIONS

Figure		Page
1	Receiver Exhaust Pressure Drop (%) versus Turbine Inlet Temp	17
2	Receiver Inlet Pressure Drop (%) versus Receiver Inlet Temp	18
3		25
4	Cycle Efficiency versus Pressure Ratio	29
5	Optimum Pressure Ratio versus Turbine Inlet Temperature	30
6	Cycle Efficiency at the Optimum Pressure Ratio versus Turbine Inlet Temperature	31
7	Receiver Inlet Temperature at the Optimum Pressure Ratio versus Turbine Inlet Temperature	33
8	Receiver Inlet Temperature versus Pressure Ratio and Turbine Inlet Temperature	34
9		37
10	Open Receiver	39
11	Windowed Receiver	40
12A	Energy Distribution	42
12B	Energy Distribution	43
13		45
14	Profile of the CPC Terminal Concentrator	48
15	Vertical Flux Component versus Position $W \cdot cm^{-2}$	52
16	Radial Flux Component versus Position $W \cdot cm^{-2}$	53
17	Total Flux versus Position $W \cdot cm^{-2}$	54
18	Spectral Energy Distribution	56
19		59
20	Window Temperature Rise Quartz Type 125 versus Window Thickness	60
21	Window Temperature Rise versus Window Thickness	61
22	Window Limit Safety Nomogram	63
23	Receiver Regimes of Operation	81

EXECUTIVE SUMMARY

Under the provisions of Task 1, Parametric Analysis, the High Temperature Solar Thermal Receiver program several receiver concepts were developed and analyzed. A review of the findings is presented in Table 1.

A comparison of concept capabilities within the range of interest shows the optimal receiver to be a windowed matrix receiver. The design offers the probability of low production cost, low risk, and compatibility with the most likely identified application, the powering of an advanced (ceramic) Brayton engine to 2600^{o}F.

The design permits optional installation of additional thermal buffering mass or a hybrid burner behind the receiver matrix.

Thermal buffer (storage) performance would be the best of the several concepts because radiation losses from storage are virtually nonexistent.

TABLE 1

Concept	Description	Window	Temperature Inlet	Temperature Outlet	Pressure Atm	Power	Storage	Weight	Risks	Cost	Rating
A	Matrix	Yes	1800	2000-3000	2-8	25-150	No	180	Low	1	1
A'	Matrix	Yes	1800	2000-3000	2-8	25-150	Yes	306	Low	2	2
B	Extended Surface Bell Jar	No	2500	2000-3000	?	?	No	131	High	4	5
C	Extended Surface Radial Fins	Yes	1800	2000-3000	2-8	25-150	Intrinsic	337	Low	3	3
D	Tubed	No	2500	2000-3000	2-8		Intrinsic	287	Intrinsic	5	4

ORIGINAL PAGE IS
OF POOR QUALITY

ORIGINAL PAGE IS
OF POOR QUALITY

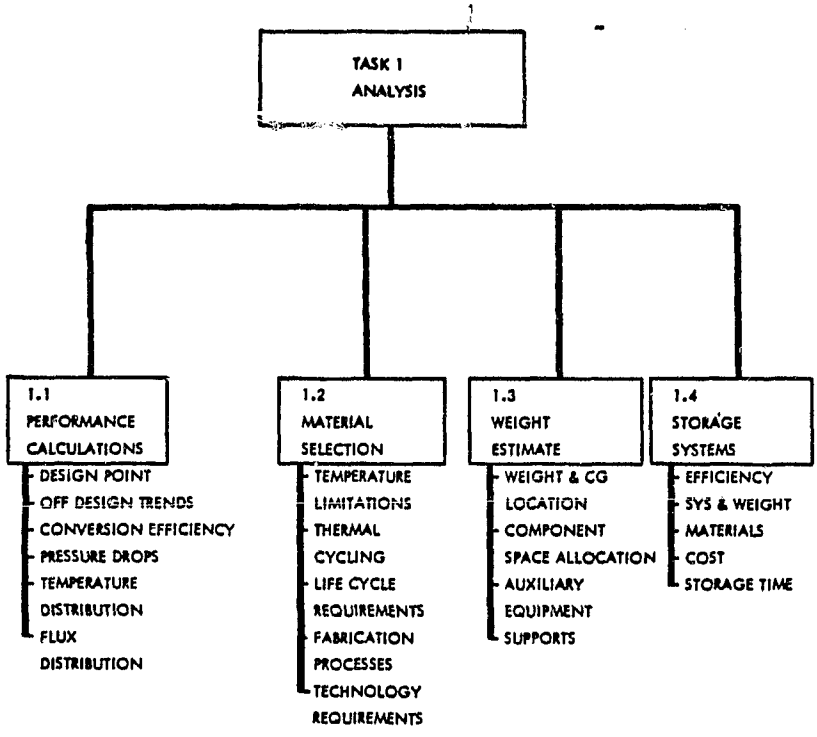

TASK 1 - STATEMENT OF WORK

(1) Task 1 - Parametric Analyses

Perform receiver parametric analysis on various design options and characterize the performance of subsystem and components for comparison and optimization purposes. The data shall be displayed to clearly show design point and off-design performance trends at various operating conditions. The result of this effort shall include, but not be limited to, the following:

(A) Preliminary receiver performance calculations and graphs related to thermal efficiency, pressure drop, cavity temperature and flux distribution.

(B) A material selection based upon thermal cycling, life-cycle requirements, cost fabrication considerations and experience in similar or comparable technologies.

(C) Weight estimate and space envelope diagram with identification of major components, physical arrangement, necessary supporting devices and auxiliary equipment.

(D) The merits of various thermal energy storage systems shall be assessed with respect to thermal efficiency, size, weight, cost and material compatibility. Storage time to be considered should be up to 3 minutes.

CONCEPTS

In accordance with the SOW and the contents of Sanders' proposal (WIPCN) for a High Temperature Solar Thermal Receiver various design options were generated for analysis and evaluation.

The decision to investigate only cavity type receivers was made at the outset. The high potential for thermal radiation losses associated with the high temperatures specified set an a priori design constraint; the active heat transfer surfaces must be enclosed within a loss limiting thermal cavity.

The proposal offered three basic design types: matrix, extended surface, and tubed receivers. Recent investigation suggests that the receiver should be categorized not only by the configuration of the active heat transfer surfaces but also by the aperture configurations.

The table below shows a cross-classification of the concepts investigated.

	Open Aperture	Windowed Aperture
Matrix	N/I	A
Extended Surface	B	C
Tubed	D	N/A

The significance of the classification is suggested by the following criteria.

First, the window substantially affects the receiver heat balance. Incoming radiation is reduced by first and second surface reflection; reradiation is reduced by 35 to 20%; and aperture convection losses are eliminated. The relative magnitude of these effects is discussed later in the window analysis section.

Secondly, the use of a window as a pressure bulkhead significantly relieves the working stresses in the active heat transfer device. This allows the use of thin walled sections which allow the heat to be convected directly off the receiving surface rather than first being conducted through a wall to a pressurized convection surface.

The open (aperture) matrix receiver was not evaluated because the pressure specifications of the contract range from 2 to 8 atmospheres. As a result of this restriction, the flow dynamics selected for the windowed matrix receiver (Concept A) were configured to use the input air for efficient window cooling. The selected flow pattern would obviously induce substantial losses through the aperture if a window were not present.

In the case of concept A, however, the impingement cooling of the window does not induce additional losses. The input air cools the rear surface of the window to its adiabatic conduction temperature. For turbine applications the receiver inlet air is always below 1800^{o}F in optical systems, so adequate window cooling is assured.

Referring to Plate A the features of the windowed matrix receiver are:

(1) Concentric inlet/output ducting reduces external heat losses.

(2) Inlet air is ducted through a formed insulation nozzle to provide a jet for window cooling and uniform flow to the ceramic matrix panels.

(3) Internal structure is provided by rigid insulation to minimize cost, weight and heat loss.

(4) External housing of carbon steel serves as a pressure vessel.

OF POOR QUALITY

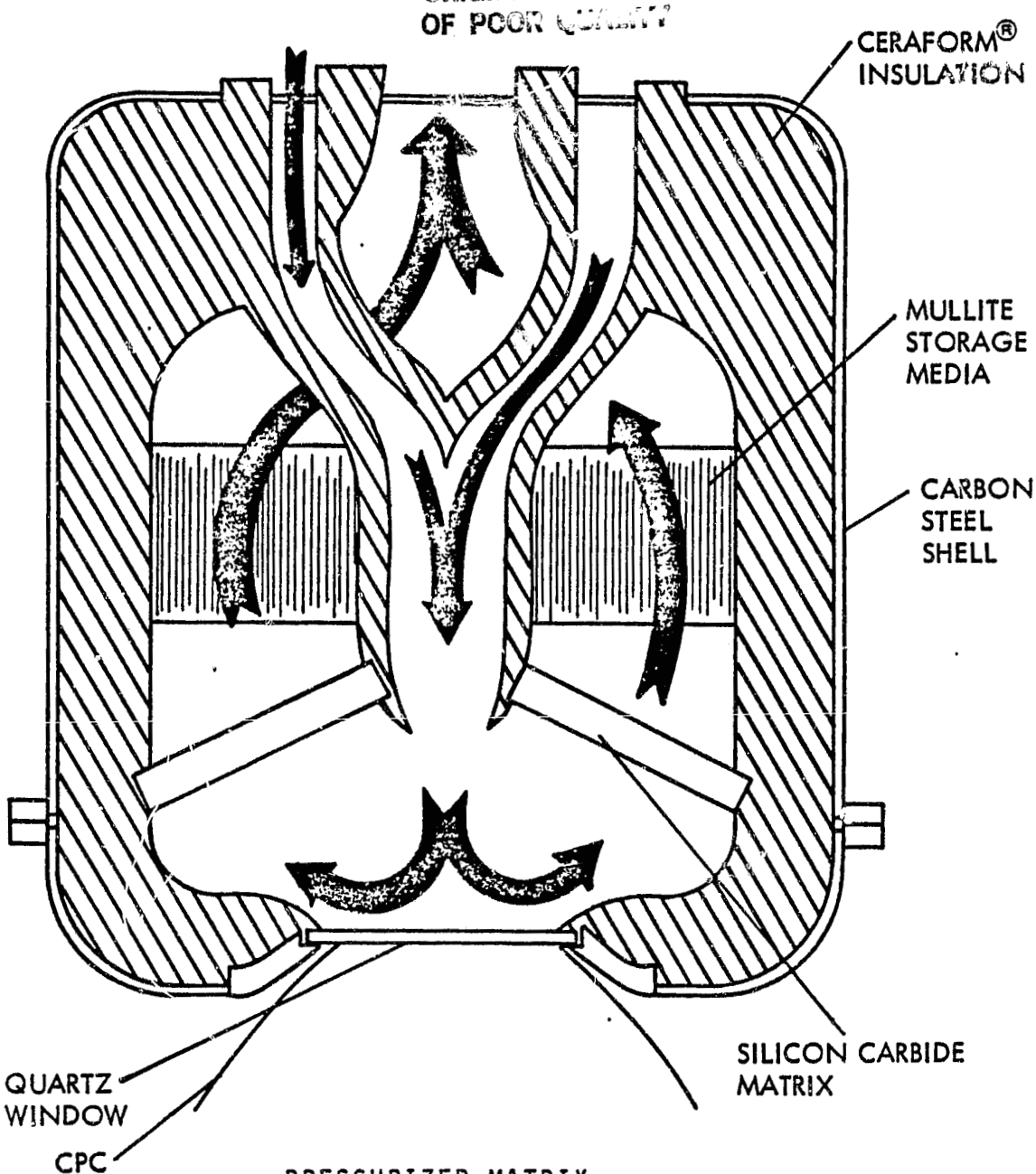

PRESSURIZED MATRIX

HIGH TEMPERATURE SOLAR THERMAL RECEIVER

ENGINEERING SKETCH

ORIGINAL PAGE IS
OF POOR QUALITY

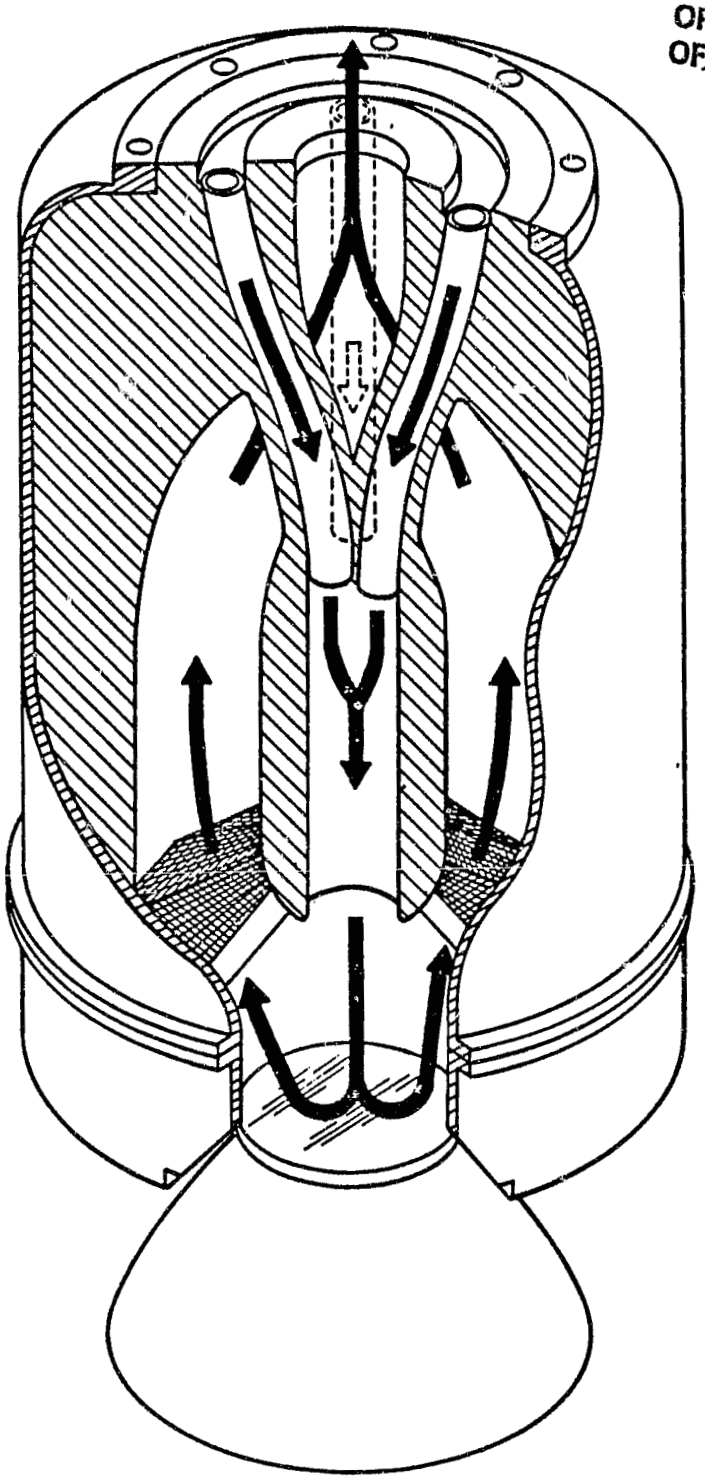

PRESSURIZED MATRIX

HIGH TEMPERATURE SOLAR THERMAL RECEIVER

PLATE A

(5) Cavity ratio of approximately 8:1 is achieved by arrangement of matrix panels in region of maximum flux. Cavity temperature $\sim 200^{o}$ above outlet air temperature.

(6) Seventy kilowatt model weighs 180 pounds as shown or 310 pounds with additional thermal buffer.

(7) Design allows for easy initial fabrication and replacement of parts.

(8) Inlet temperatures are limited to approximately $1800^{o}F$ by window cooling requirements, unless a higher temperature material like sapphire is considered. In view of the turbine application parameters investigated, however, this is a relatively inconsequential limitation. Process heat applications are not likely to impose more severe inlet conditions because process heat recuperaters capable of operation at exhaust temperatures are nonexistent, unless the Sanders ceramic TSM is considered.

The open extended surface receiver shown on Plate B consists of a single walled ceramic pressure vessel which resembles an externally finned bell jar. System working pressure is contained between the ceramic vessel at the cavity interior and an outer housing of carbon steel, which is protected by formed rigid insulation.

Principle features of this concept are highlighted below:

(1) Concentric inlet/outlet ducting reduces external heat losses.

(2) Inlet air fully jackets receiver cavity to minimize wall losses.

(3) Inlet baffle directs inlet air to external (pressurized) side of bell jar fins.

ORIGINAL PAGE IS
OF POOR QUALITY

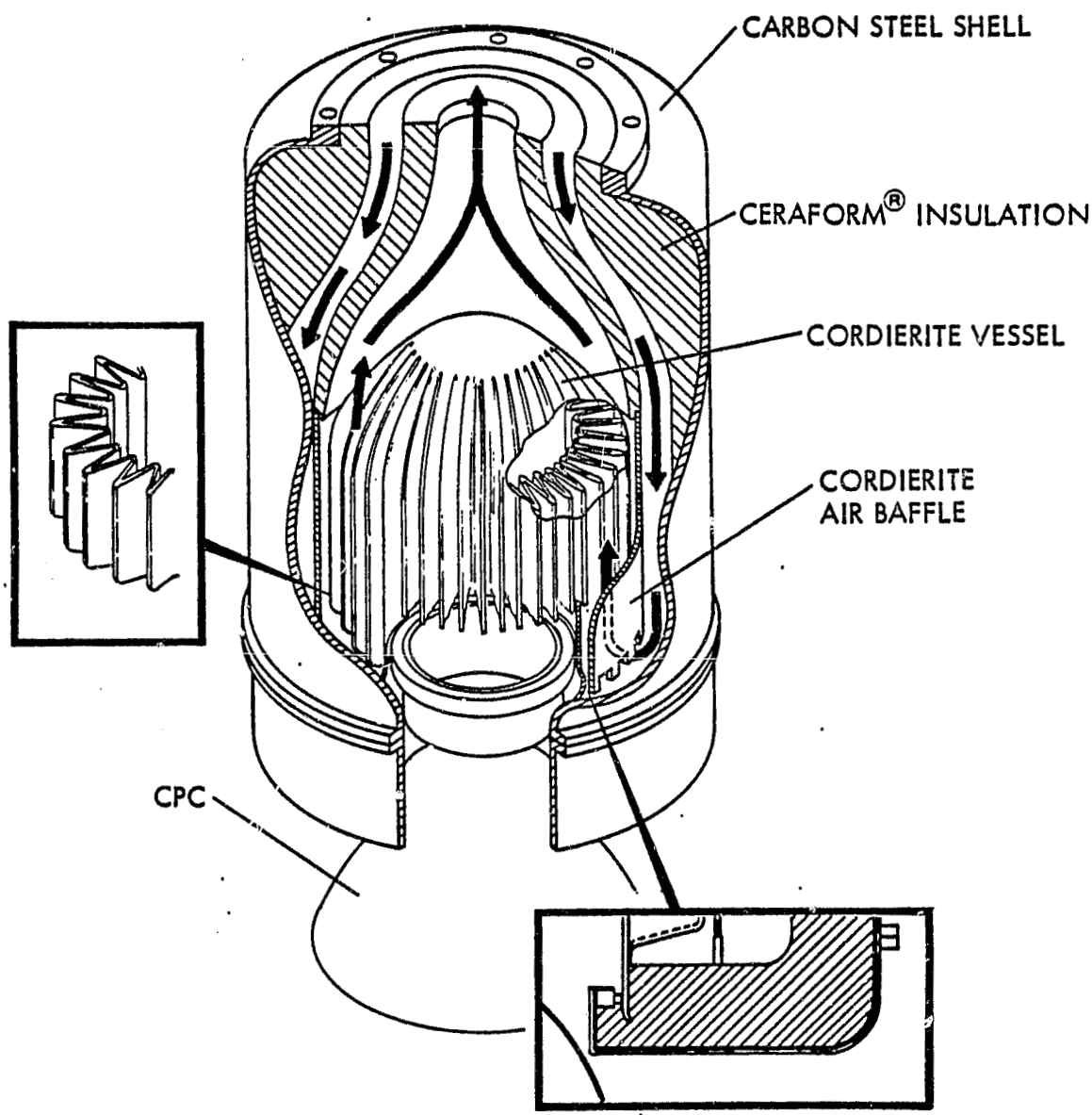

OPEN EXTENDED SURFACE RECEIVER

PLATE B

(4) Internal side of bell jar fins (at atmospheric pressure) are hollow to increase solar absorption area and to decrease temperature gradients in fins.

(5) Expansion of receiver element is allowed by sliding seal at base of bell jar in region protected from direct solar and diffuse thermal radiation.

(6) Cavity ratio of approximately 10:1 is achieved by convoluting cavity wall. Cavity temperature $\sim 250^{0}$ above outlet air temperature.

(7) Seventy kilowatt model weighs ~130 pounds, with minimal thermal buffering.

(8) Design is simplest of the investigated concepts for assembly. Key issues lie in the slip casting and subsequent firing of the convoluted bell jar.

(9) Design provides for easy maintenance-but in the event of jar failure, the entire monolith would probably have to be replaced.

The windowed extended surface receiver shown on Plate C share many design features with the windowed matrix receiver. The principle difference is the integral thermal buffering provided by the plate fins. Features are:

(1) Concentric inlet/outlet ducting to minimize external heat loss.

(2) Inlet air is ducted through formed insulation nozzle to provide a jet for window cooling and uniform flow to the fins.

(3) Internal structure is provided by rigid insulation to minimize cost, weight and heat loss.

ORIGINAL PAGE IS
OF POOR QUALITY

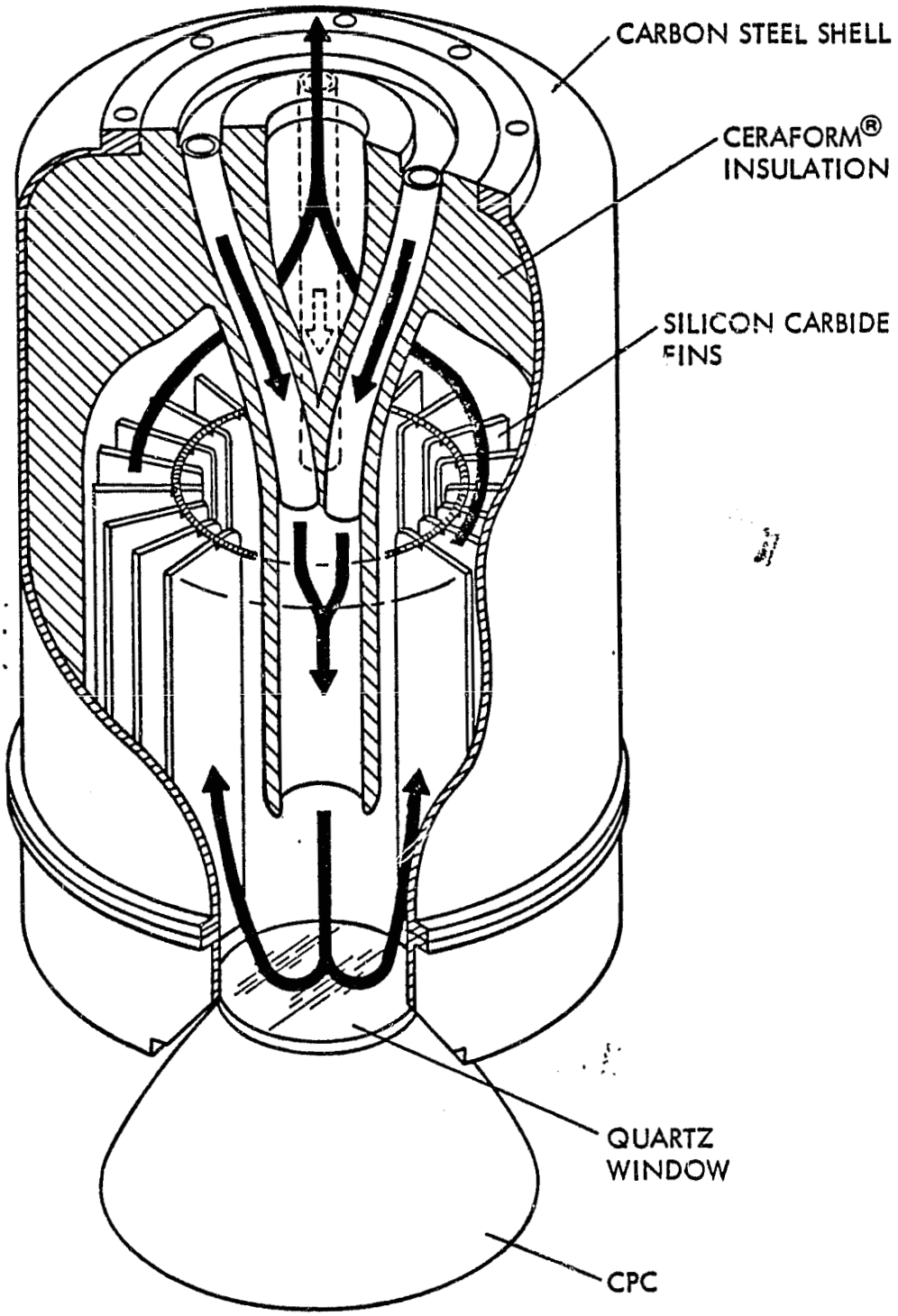

WINDOWED EXTENDED SURFACE RECEIVER

PLATE C

(4) External housing of carbon steel serves as pressure vessel.

(5) Cavity ratio of approximately 100:1 minimizes cavity temperature rise above output air temperature. Cavity temperature $\sim 150^{\circ}$ above outlet air is expected.

(6) Seventy kilowatt model weighs ~340 pounds with thermal buffering.

(7) Inlet temperatures are limited to approximately $1800^{\circ}F$ by window (quartz) requirements, but as noted earlier, this is a relatively inconsequential limitation.

Probably the most controversial design is the tubed receiver shown on Plate D. The design is not radically different from other well publicized designs in the industry. Acknowledged points of commonality are the double row of vertical ceramic tubes, the use of preloaded ball socket joints and the insulated air distribution plenum.

There are incorporated, however, several design details which differ from previously published work on similar receivers as far as known by this investigator.

(1) A single distribution and collection plenum is provided. Internal insulation protects that vessel from the high working temperatures while simultaneously forming separate input and outlet flow channels of varying cross-section.

(2) The vertical tubes are not joined by a fixed U-pipe but are connected by a floating ball and socket U-fitting. This arrangement allows for differential expansion of the outer (cool inlet) pipe and the inner (hot outlet) pipe without requiring sliding seals and without inducing bending moments.

ORIGINAL PAGE IS
OF POOR QUALITY

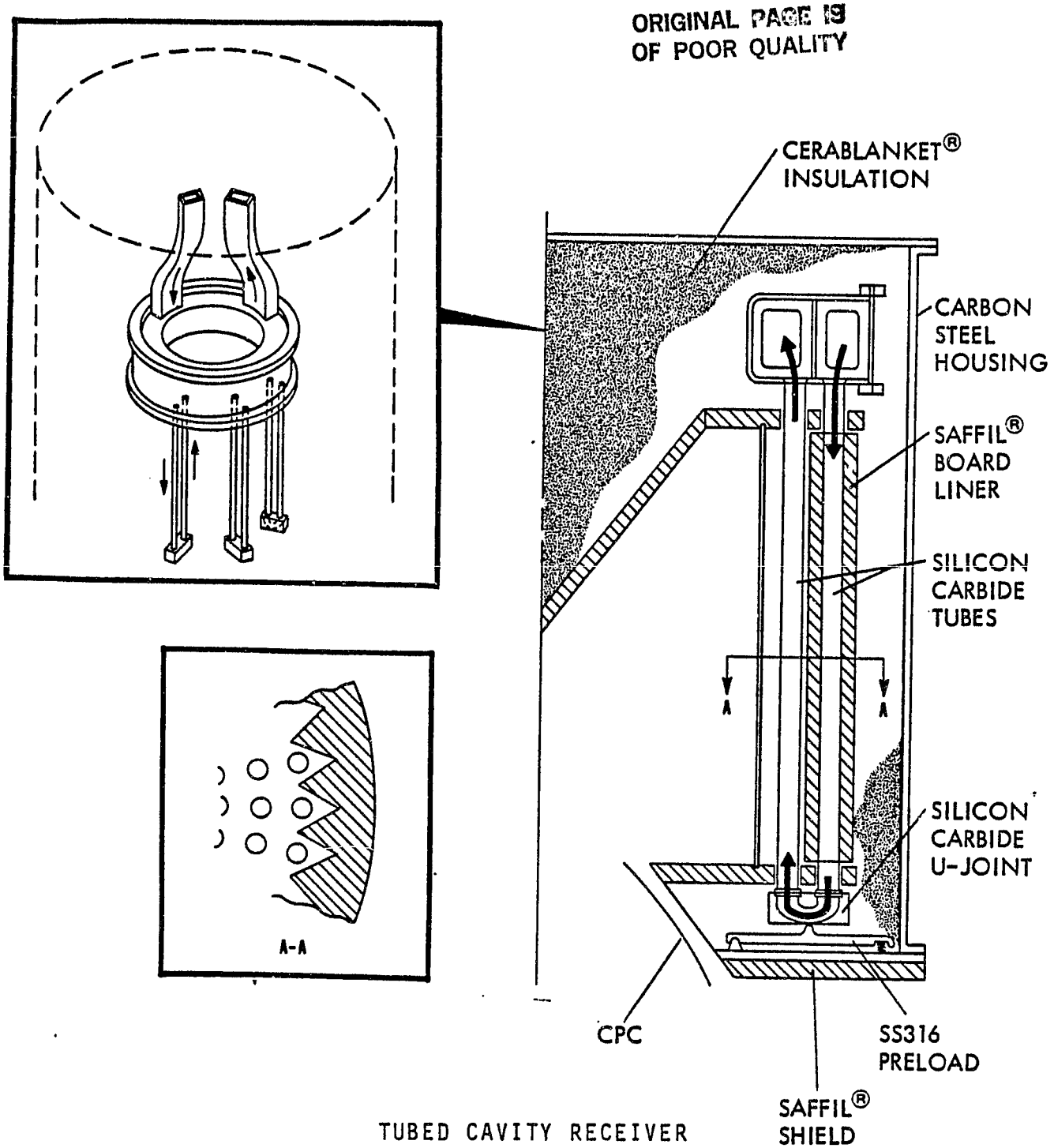

TUBED CAVITY RECEIVER

PLATE D

(3) A thin curved ceramic sun shield is provided in front of the inner tubes to clock direct radiation. This shield will reradiate to the cavity at 500 watts cm^{-2} when heated to 2600°F. Its rear surface is convex to mitigate the reradiation toward the shielded tube.

(4) The insulated wall of the cavity is cusped to preferentially radiate and reflect towards the rear facing surface of nearby tubes.

(5) The rooftop of the cavity is deeply depressed to redirect impinging radiation toward the active tube surfaces rather than out the aperture.

(6) Weight of the receiver is approximately 300 pounds with intrinsic thermal buffering provided by the mass of the tubes.

(7) The receiver offers a relatively low risk configuration for containment of pressurized gases, but at the apparent expense of complicated assembly and high cost components.

RECEIVER PRESSURE DROPS

Pressure drops for the windowed matrix receiver were calculated for base line conditions of:

Mass flow = 0.4 lbs sec^{-1} and
Pressure = 4 atmospheres

Pressure drops were calculated for a range of receiver inlet temperatures and outlet temperatures.

The data and curves are presented below.

HOT (Figure 1)

(psf)	P_R 2	3	4	5	6	7	8
2000	0.824	0.550	0.412	0.330	0.274	0.235	0.206
2500	2.930	1.950	1.465	1.172	0.970	0.837	0.732
3000	8.360	5.570	4.180	3.440	2.780	2.380	2.100
$\left(\frac{\Delta P}{P}\right)$							
2000	0.040 0.020	0.016 0.008	0.008 0.004	0.006 0.003	0.004 0.002	0.003 0.015	0.0024 0.0012
2500	0.140 0.070	0.060 0.030	0.034 0.017	0.022 0.011	0.014 0.007	0.010 0.005	0.008 0.004
3000	0.380 0.019	0.174 0.087	0.100 0.050	0.064 0.032	0.044 0.022	0.032 0.016	0.024 0.012

COLD (Figure 2)

(psf) T_2"	P_R 2	3	4	5	6	7	8
1000	0.810	0.540	0.406	0.324	0.270	0.232	0.203
1500	1.500	1.000	0.750	0.600	0.500	0.428	0.375
2000	2.750	1.830	1.033	1.100	0.920	0.780	0.680
$\left(\frac{\Delta P}{P}\right)$							
1000	0.038 0.019	0.016 0.008	0.008 0.004	0.006 0.003	0.004 0.002	0.003 0.0015	0.0024 0.0012
1500	0.075 0.035	0.030 0.015	0.018 0.009	0.011 0.0056	0.008 0.004	0.0056 0.0028	0.0044 0.0022
2000	0.128 0.064	0.056 0.028	0.034 0.017	0.020 0.010	0.014 0.007	0.010 0.0052	0.008 0.004

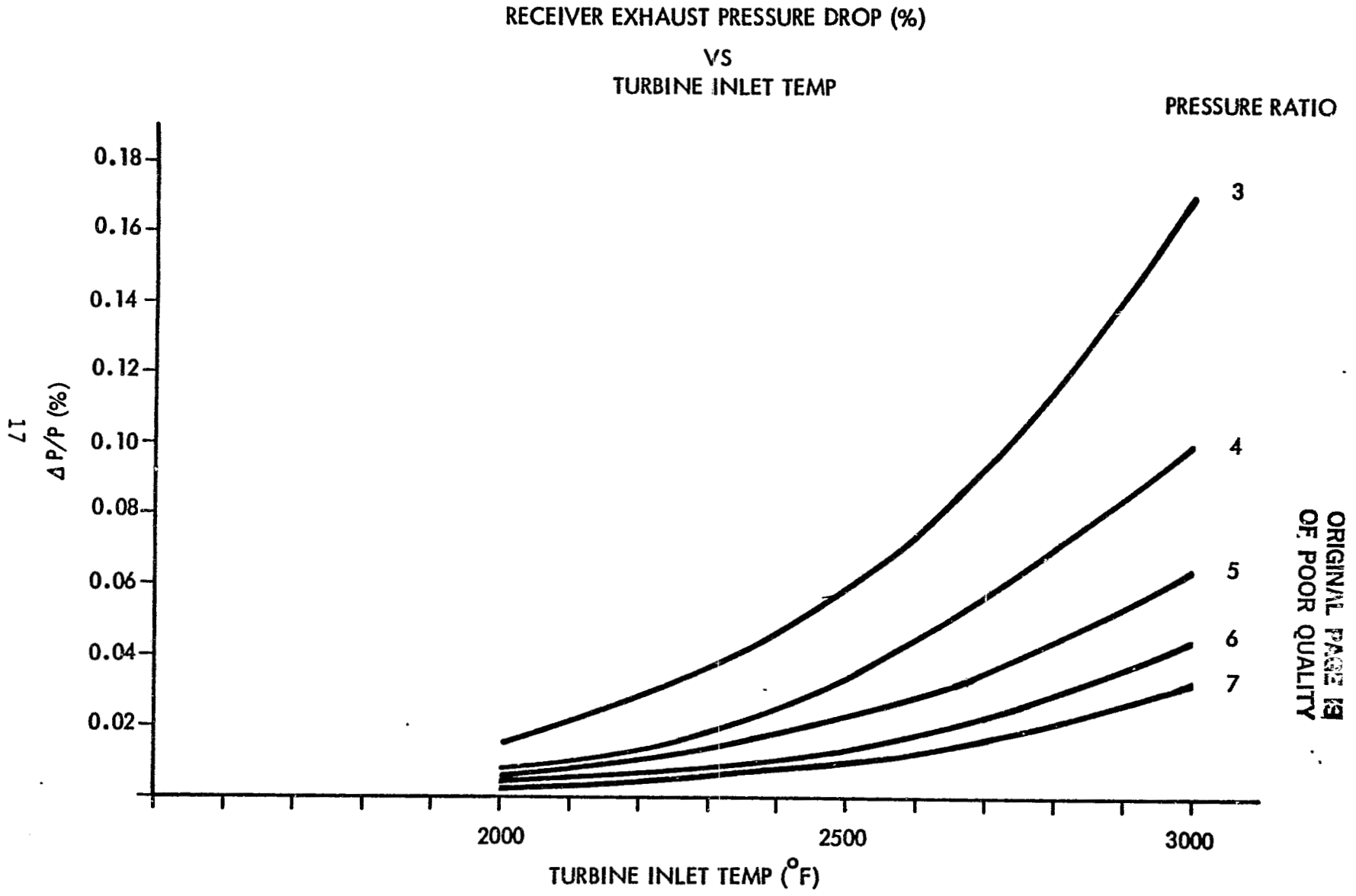

ORIGINAL PAGE IS
OF POOR QUALITY

Figure 1.

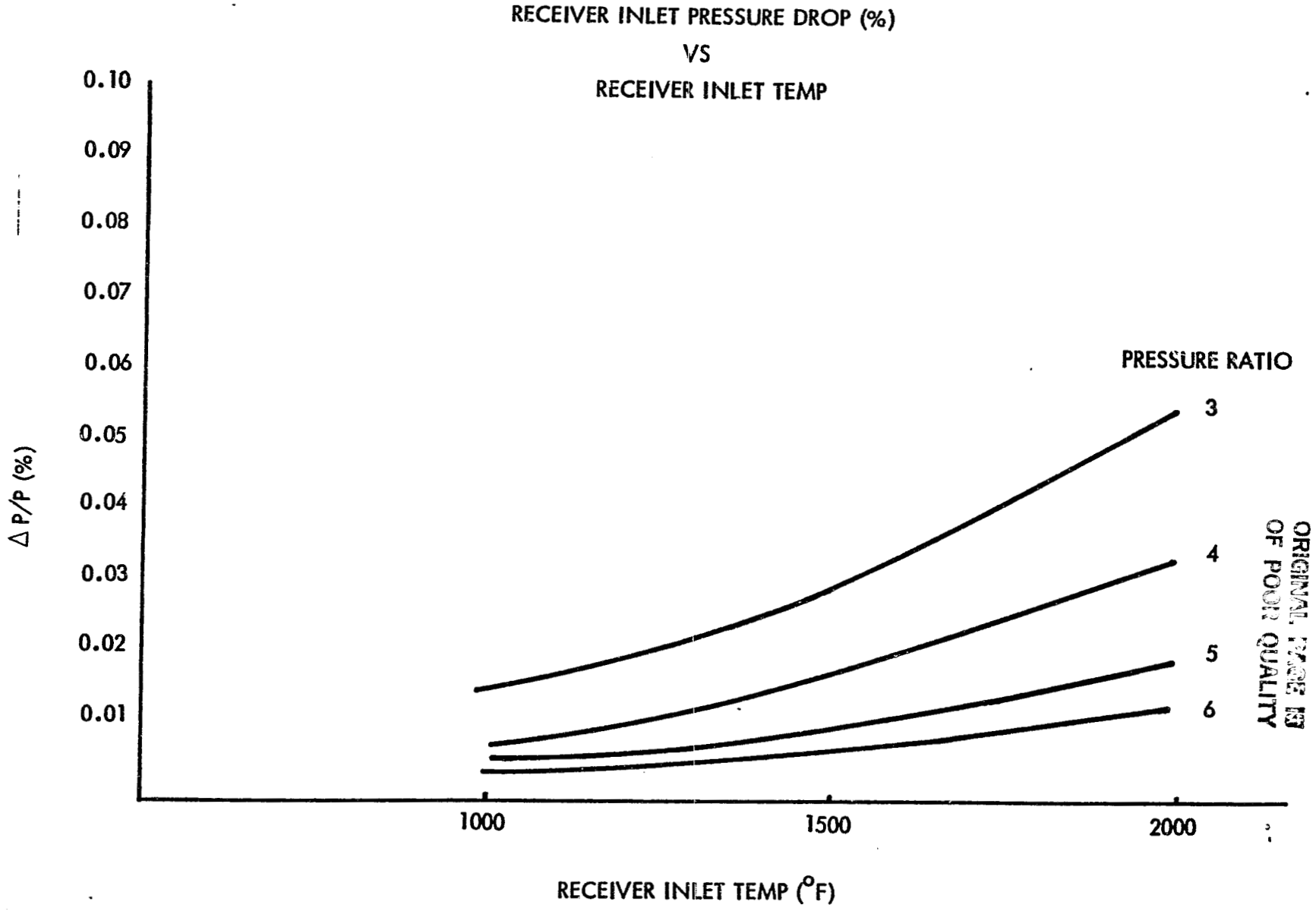
RECEIVER INLET PRESSURE DROP (%)
VS
RECEIVER INLET TEMP
0.10
0.09
0.08
0.07
0.06
0.05
0.04
0.03
0.02
0.01
ΔP/P (%)
PRESSURE RATIO
3
4
5
6
1000
1500
2000
RECEIVER INLET TEMP (°F)
ORIGINAL PAGE IS
OF POOR QUALITY

Figure 2.

WORKING FLUID EFFECTS ON PRESSURE DROPS

The candidate working fluids specified in the statement of work are air, nitrogen and helium. The pressure drop and heat transfer effects of the diverse physical properties of the three working fluids were investigated for a 56 kW receiver operating between 1750°F inlet and 2500°F outlet. A qualitative summary of the findings is presented below:

Parameter	Air	Nitrogen	Helium
Pressure Drop	Highest	High	Lowest
Tube Temp Rise	Mid	Lowest	Highest
Limitations, SiC	Mid	Most	Least
Limitations, Oxides	Least	High	Mid
Leakage Tolerance	Highest	Mid	Least
Leak Potential	Lowest	Mid	Highest

A review of this table shows that helium does offer advantages in low pressure drops and is nonreactive with silicon carbide, but is otherwise less advantageous that either air or nitrogen. Nitrogen offers slight heat transfer advantages over air but tends to react with silicon carbide to form silicon nitride. Air, as a working fluid, is inexpensive (virtually free except for possible pretreatments such as filtering which might be required in dusty or industrial environments), is easily replaced, and is generally nonreactive with α-sintered silicon carbide and metal oxide ceramics. Finally, air, as a heat transfer fluid, is only slightly less efficient that either nitrogen or helium. The advantages of air significantly outweigh its disadvantages.

The important finding of the analysis is the requirement that a tubed receiver must be significantly larger than a matrix receiver of the same power. The tubed receiver is larger by approximately a $\sqrt{10}$ factor than the matrix receiver. In other words, a matrix receiver

can be practicably built with a much higher (active) surface/volume ratio than can a tubed receiver.

Whereas the 56 kW tubed receiver has a cavity radius of ∿27 inches, a 56 kW matrix receiver cavity need only have an 8.5 inch radius.

The quantitative results of the pressure drop analysis for the tubed 56 kW receiver operating with the three different working fluids is presented in Table 1 below. Note that the power level, 56.2 kW, is constant throughout the analysis and corresponds to an air charged receiver flowing 0.25 lb/sec^{-1} with inlet and outlet temperatures of 1750°F and 2500°F, respectively.

TABLE 1. PRESSURE DROP SUMMARY

PHYSICAL PARAMETERS			WORKING FLUID		
Property	Symbol,	Units	Air	Nitrogen	Helium
Inlet Temp	T_I,	^oF	1750.0	1750.	1750.
Output Temp	T_O,	^oF	2500.0	2500.	2500.
Mass Flow	$\dot{m}$,	lb/sec^{-1}	0.250	0.241	0.0853
Specific Heat @ 1750^oF	Cp_I,	BTU/lb^{-1}	0.279	0.288	1.25
Specific Heat @ 2500^oF	Cp_O,	BTU/lb^{-1}	0.289	0.301	1.25
Enthalpy Change	ΔH,	BTU/lb^{-1}	213.	221.	624.
Power	P_M,	kW	56.2	56.2	56.2
Power	P_E,	BTU/hr^{-1}	1.92E5	1.92E5	1.92E5
Pressure	p,	lb/ft^{-2}	6480.	6480.	6480.
Gas Constant	R,	$ft/^oF^{-1}$	53.4	55.2	386.
Density @ 3 ATM, 1750^oF	ρ_I,	lb/ft^{-3}	0.055	0.053	0.0076
Density @ 3 ATM, 2500^oF	ρ_O,	lb/ft^{-3}	0.041	0.040	0.0057
Volumetric Flow, 1750^oF	$\dot{V}_I$,	ft^3/sec^{-1}	4.54	4.55	11.2
Volumetric Flow, 2500^oF	$\dot{V}_O$,	ft^3/sec^{-1}	6.10	6.02	15.0
Tube ID	D_H,	inches	0.5	0.5	0.5
Number of Tube Pairs	N,		96.0	96.0	96.0
Total Flow ARea	A,	ft^2	0.131	0.131	0.131
Velocity, RMS	$\bar{V}$,	ft/sec^{-1}	41.0	40.7	101.0
Viscosity	μ,	$lb/hr^{-1}/ft^{-1}$	4.39E2	4.13E2	4.76E2
Reynold's Number	N_R		6.72E3	6.87E3	2.12E3
Convective Film Coefficient	h,	$BTU/hr^{-1}/ft^{-2}/^oF^{-1}$	8.57	9.15	8.00
Active Length of Tubes	ℓ,	ft	5.0	5.0	5.0
Active Area of Tubes	A_c,	ft^2	62.8	62.8	62.8
Film Drop	ΔT,	^oF	356.0	334.0	382.0
Friction Factor	f,		0.0091	0.009	.0075-.011
Pressure Drop	Δp,	lb/ft^{-2}	88.0	83.0	61.0-90.0
% Pressure Drop	$\Delta p/p$,	%	1.4	1.3	.94-1.4

BRAYTON CYCLE EVALUATION

ENGINE PARAMETERS

The high temperature receiver (HTSR) has been investigated to replace the burner in a Brayton cycle. A set of realistic component efficiencies and cycle conditions have been specified to determine the best operating range of the cycle. All four components of the Brayton engine, namely compressor, turbine, burner and heat exchanger have been developed extensively over the past 30 years. But now, emphasis is being placed to increase cycle efficiencies by raising turbine inlet temperatures. In most industrial and utility applications turbines have been limited to 100-1500^{o}F temperatures. But with advances in materials technology and requirements of high performance aircraft, turbine inlet temperatures have risen to 2300-2700^{o}F in some applications. It is conceivable to use this technology and apply it to solar powered Brayton cycles. For this exercise, turbine adiabatic efficiency of 87% has been assumed, by varying turbine inlet temperatures from 2000^{o}F to 3000^{o}F.

The design of the compressor is very critical to the overall performance of the Brayton engine since it consumes 60 to 80% of the turbine output. Therefore, for a value to use in rough estimates it is safe to think of the net power of the system as amounting to 20 to 40% of the turbine output. For the present analyses a compressor efficiency of 80% is assumed.

The development of high temperature and pressure metalic heat exchanger has been shown in development. Therefore, most high temperature Brayton engines have been designed unrecuperated and work at high pressure ratios to obtain efficiency improvements. Again, with advances in materials technology or by use of ceramic recuperators Brayton engines could operate at much lower pressure ratios with real improvements in cycle efficiencies. The parametric analysis is done at three recuperator effectivenesses of 0, 0.5 and 0.9 to evaluate cycle performance.

HTSR replaces the burner in the Brayton engine. Based on the parametric study done on the receiver, a 4% thermal loss has been incorporated in cycle analysis. Furthermore, the pressure drops of the system has been estimated to be 2% during the heat addition process and 5% during the heat rejection. The effect of this pressure drop is to reduce the available pressure ratio across the turbine and hence reducing the cycle efficiency. The range of pressure ratios across the compressor has been varied from 2 to 8 atmospheres in an attempt to obtain the optimum pressure ratio for engine operation at various turbine inlet temperatures and recuperator effectivenesses.

The compressor inlet temperature has been selected conservatively at $100^{o}F$. By lowering the inlet temperature to $50^{o}F$ 1-2% in cycle efficiency improvement can be expected.

An important byproduct of the cycle analysis, was the determination of receiver inlet temperatures, at various operating conditions. Its value was determined based on component efficiencies and compressor and turbine inlet temperatures. Based on its magnitude, the receiver efficiency can be crudely calculated.

Even though the mass flow rate does not enter directly in the efficiency calculations a value of 0.4 lb/sec has been selected based on the available solar power and the expected temperature rise across the receiver.

METHOD OF ANALYSIS

A computer program was written to evaluate the state conditions of the Brayton cycle from the Laws of Thermodynamics. Starting from known quantities of compressor inlet and turbine inlet temperatures and component efficiencies each state; namely, temperature pressure and enthalpy have been evaluated upstream and downstream of the Brayton cycle components. Once the state conditions have been determined, cycle efficiency

is calculated. In addition, the net turbine and compressor work is calculated based in a given air flow rate through the engine and finally, the output net (kw) is calculated taking into account all parasitic losses in the cycle.

Figure 3 shows the block diagram and the T-S diagram with all the pertinent state points. The compressor operating through a pressure ratio of $P_2'/P1$ delivers air having an enthalpy of h_2', a higher value than for point (2) because of compressor inreversibilities. Heating in the recuperator may raise the temperature and enthalpy to 2" with the combustor or (HTSR) bringing the temperature to T_3. Pressure losses from 2' to 3 reduce the pressure available at the turbine inlet to the lower value P_t. Expansion now proceeds in an irreversible turbine to exhaust pressure of P_e and a final state point 4' regenerator, cooling to 4", or they can be discharged direct to atmosphere. The turbine exhaust pressure P_c is higher than the free discharge pre-sure P_1. The effect of regenerative heating of the compressed gas is clearly shown on the T-S diagram. The gases at 4' are sufficiently hot to heat the compressed gas of 2' to 2", with the hot gases at the same time cooling to 4". In the limit, the hot gases from 4' could be cooled until they essentially reach the temperature at 2'. This is the ideal recuperator and it would require an infinit surface area. Therefore, it is used as a datum to compare recuperator effectivenesses.

In actual heat transfer equipment, recuperator effectiveness for commercial design ranges from 0.5 to 0.75. However, it is possible to design for higher values of effectiveness approaching 0.85 to 0.90. In general, counterflow design is preferable and terminal temperature differences of not less than 50^0 are employed. Where the generator is not adiabatic, a portion of the thermal energy of the warm gases is dissipated and the surroundings. Energy lost in this way produces essentially the equivalent of a unit operating with a lower effectiveness.

ORIGINAL PAGE IS
OF POOR QUALITY

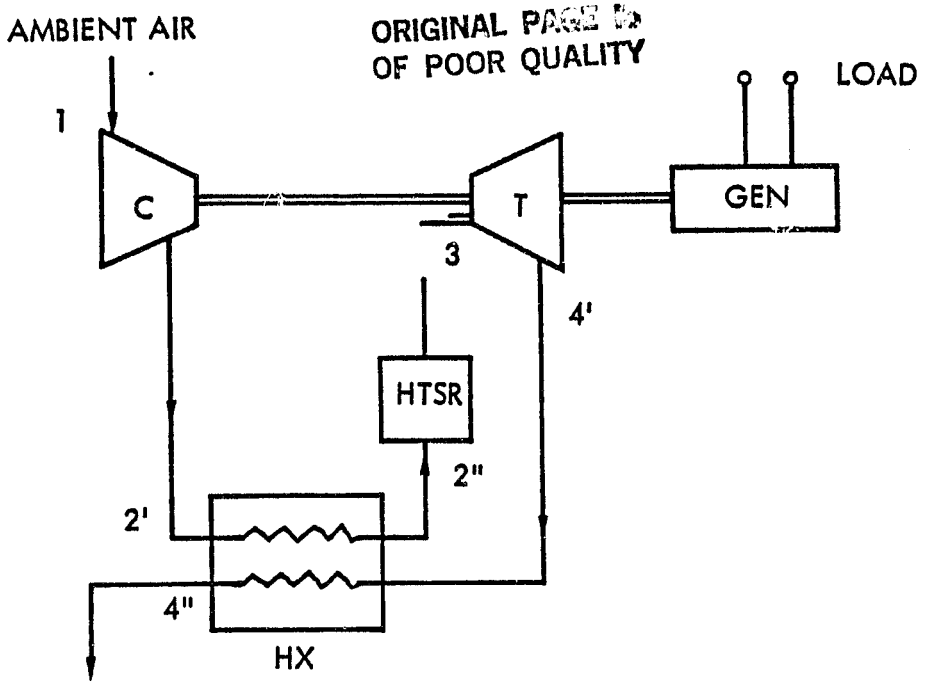

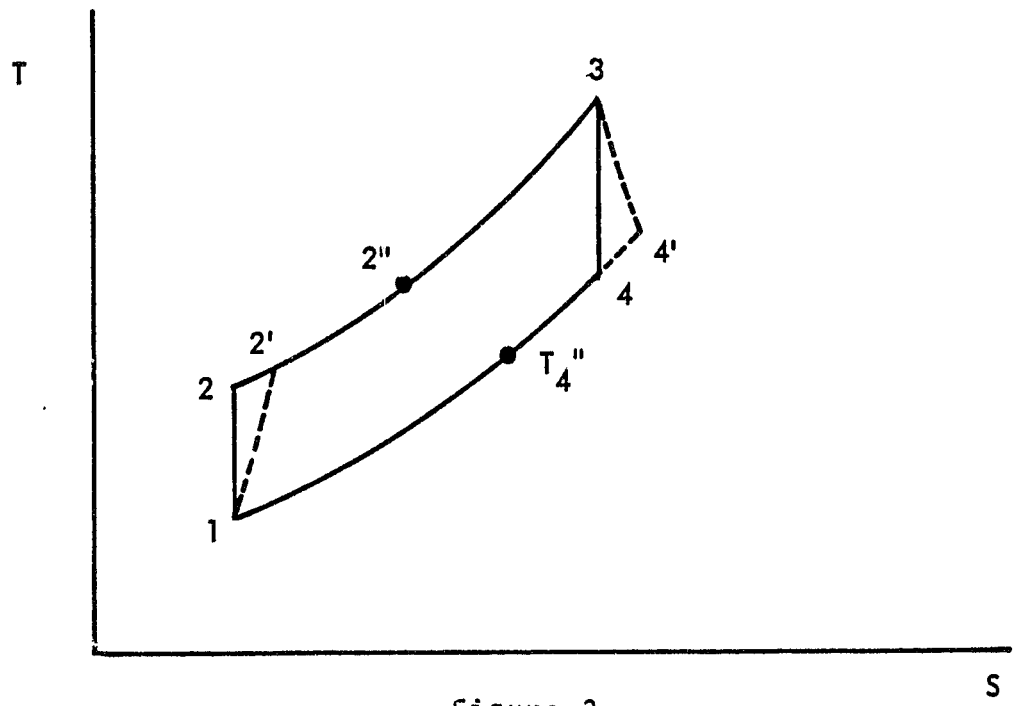

Figure 3.

RESULTS

The thermal efficiency of the Brayton cycle depends on the mean effective temperatures of heat addition and rejection. Assuming atmospheric temperature of T_1, it follows that T_2 will also be fixed for a given pressure ratio. Increasing the turbine inlet temperature T_3, will raise the mean effective temperature of heat addition. However, this will also raise the mean effective temperature of heat rejection since T_4 will be increased. The net result is an increase in thermal efficiency. Therefore, for the ideal Brayton cycle, the thermal efficiency is a fraction of the highest temperature of heat addition as shown by equation (1).

$$\eta = \frac{T_3 - T_4}{T_3} \tag{1}$$

By using a recuperator, the mean effective temperature during heat addition is raised while lowering the mean temperature during heat rejection, thereby increasing the thermal efficiency of the cycle. Or, looking at it another way, less heat is supplied from the heat source and less rejected to the heat sink. This effect is clearly shown in Figure 4 where increasing turbine inlet temperatures, invariably improves cycle efficiency.

If the pressure ratio is increased while keeping T_3 and T_1 constant, T_2 will be increased with the result that the mean effective temperature of heat addition also will be increased. The turbine exhaust temperature T_4 will be decreased, causing a corresponding decrease in the mean effective temperature of heat rejection. The net effect again is an increase in thermal efficiency as shown by equation (2).

$$\eta = 1 - \left(\frac{P_1}{P_2}\right)^{\frac{K-1}{K}} = 1 - \frac{1}{(P)^{\frac{K-1}{K}}} \tag{2}$$

In contrast to the simply unrecuperated Brayton engine the efficiency is improved at lower pressure ratios for recuperated engines. This is shown by equation (3).

$$\eta = 1 - \frac{T_1}{T_3} (r_p)^{\frac{K-1}{K}}$$

Theoretically, a pressure ratio of unity would raise the thermal efficiency to that of the Carnot cycle.

The effect of peaking in cycle efficiency is pronounced in Figure 4 when the effectiveness of the recuperator is 0.9 for a parameter of turbine inlet temperatures. For the 50% recuperated cycle peaking would also occur but at higher pressure ratios (8-9) while there is no peaking for the unrecuperated engine. For this reason, a recuperated engine is usually designed to operate at lower pressure ratios than an unrecuperated one. Therefore, it is a poor practice to add a recuperator to an already inefficiently designed simple cycle Brayton engine.

Figure 5 is a cross plot of Figure 4 showing the optimum pressure ratio versus turbine inlet temperatures for the case of 90% recuperation. The optimum pressure ratio is increased with turbine inlet temperatures. This fuel is particularly significant since with constant speed compressors the pressure ratio is substantially constant and output reduction is normally achieved by reducing turbine inlet temperatures. Therefore, poor part load performance of the Brayton cycle can be expected.

In Figure 6 cycle thermal efficiency versus turbine inlet temperatures are plotted for various recuperator effectivenesses. As shown earlier, the effect of raising the mean temperature of heat addition by raising turbine inlet temperature and by reducing the quantity of heat addition by the burner results in improved cycle efficiency. This effect is the smallest in the unrecuperated engine where a 4% efficiency improvement is obtained in going from 2000 to 3000^{o}F while an 11% improvement is obtained with 90% recuperated engines. Furthermore, by

TABLE 2. BRAYTON PERFORMANCE DATA

T_1T (^oF)		PR=2			PR=3			PR=4			PR=5			PR=6			PR=7			PR=8		
		0	0.5	0.9	0	0.5	0.9	0	0.5	0.9	0	0.5	0.9	0	0.5	0.9	0	0.5	0.9	0	0.5	0.9
2000.	T_2''	266	978	1560	366	945	1417	445	929	1324	509	921	1257	563	917	1205	614	916	1163	658	917	1128
	η %	.87	16	36.3	15.2	22.9	40.7	18.5	26.3	40.9	20.7	28.1	40.2	22.3	29	39.1	23.4	29.5	37.8	24.3	29.7	36.5
2200.	T_2''	268	1070	1724	368	1030	1571	446	1010	1470	511	999	1398	567	993	1341	616	990	1296	659	989	1258
	η	9.8	15.1	37.4	15.4	23.4	42.6	18.9	27.1	43.4	21.2	29.2	43	22.9	30.4	42.1	24.2	31.2	41.2	25.2	31.6	40.1
2400.	T_2''	269	1165	1896	370	1118	1729	448	1094	1621	513	1080	1543	568	1071	1482	617	1066	1433	661	1064	1302
	η	9.5	15.7	37.5	15.3	23.4	43.7	18.8	27.3	45	21.3	29.7	45	23.1	31.2	44.5	24.5	32.1	43.7	25.6	32.8	42.9
2600.	T_2''	271	1249	2048	371	1200	1876	449	1171	1760	514	1154	1677	570	1144	1612	619	1137	1560	662	1132	1516
	η	10	16.5	39.3	15.7	24.1	45.7	19.3	28.2	47.2	21.9	31.7	47.3	23.8	32.4	47	25.3	33.5	46.4	26.4	34.2	45.7
2800.	T_2''	273	1324	2183	373	1281	2022	451	1244	1891	515	1223	1801	571	1211	1733	620	1202	1678	664	1197	1632
	η	11.1	18.3	42.9	15.9	24.5	47	20.1	29.4	49.6	22.7	32	49.8	24.7	33.7	49.6	26.2	34.9	49.1	27.4	358	48.5
3000.	T_2''	274	1401	2522	37.4	1342	2132	452	1321	2031	517	1289	1926	572	1274	1847	621	1264	1789	665	1257	1741
	η	11.9	19.5	45.5	17.6	26.8	50.5	20.2	29.7	50.7	23.7	33.4	52.2	25.7	35.2	52	27.2	36.4	51.6	28.5	37.4	51.1

ORIGINAL PAGE IS
OF POOR QUALITY

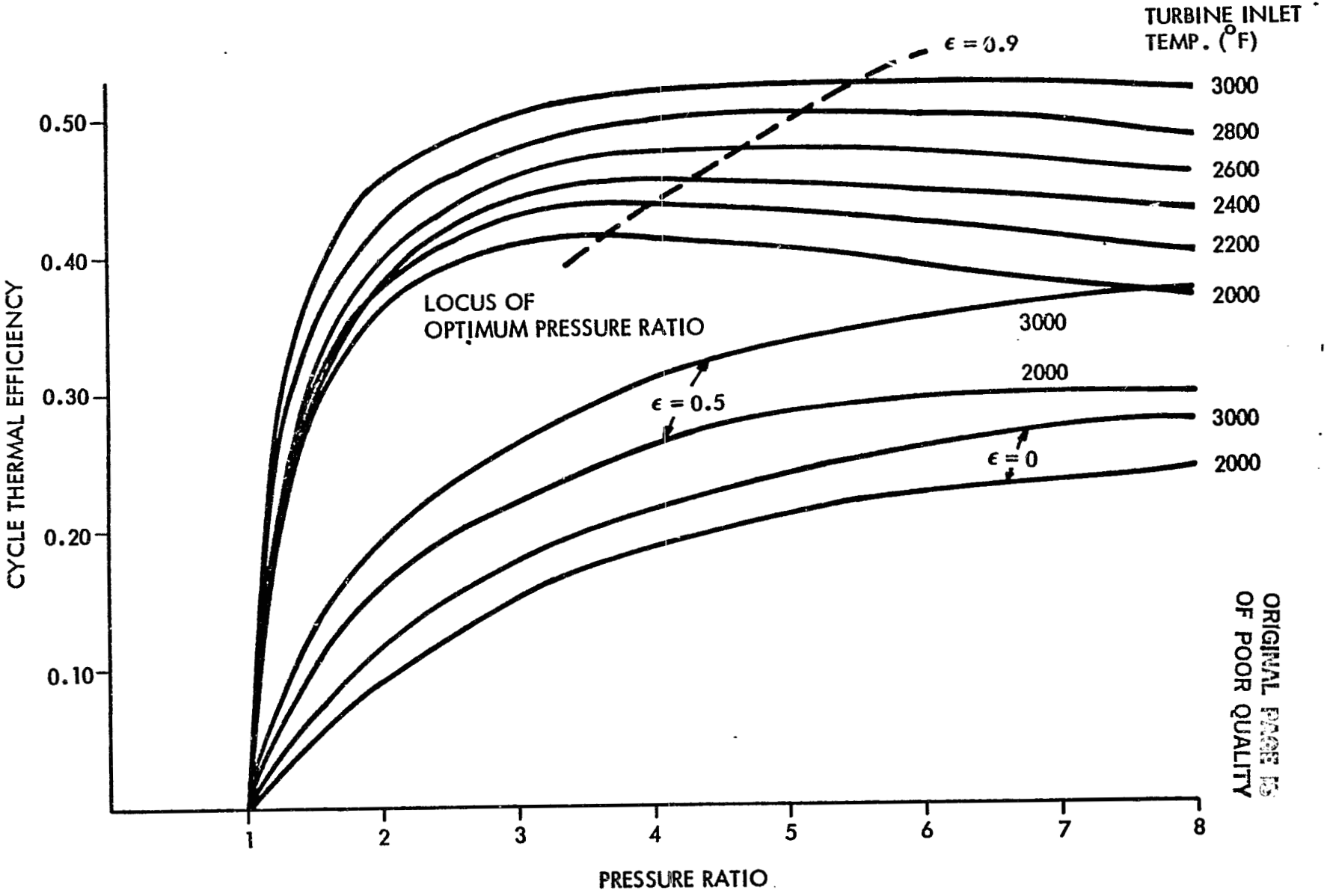

ORIGINAL PAGE IS OF POOR QUALITY

Figure 4. Cycle Efficiency versus Pressure Ratio

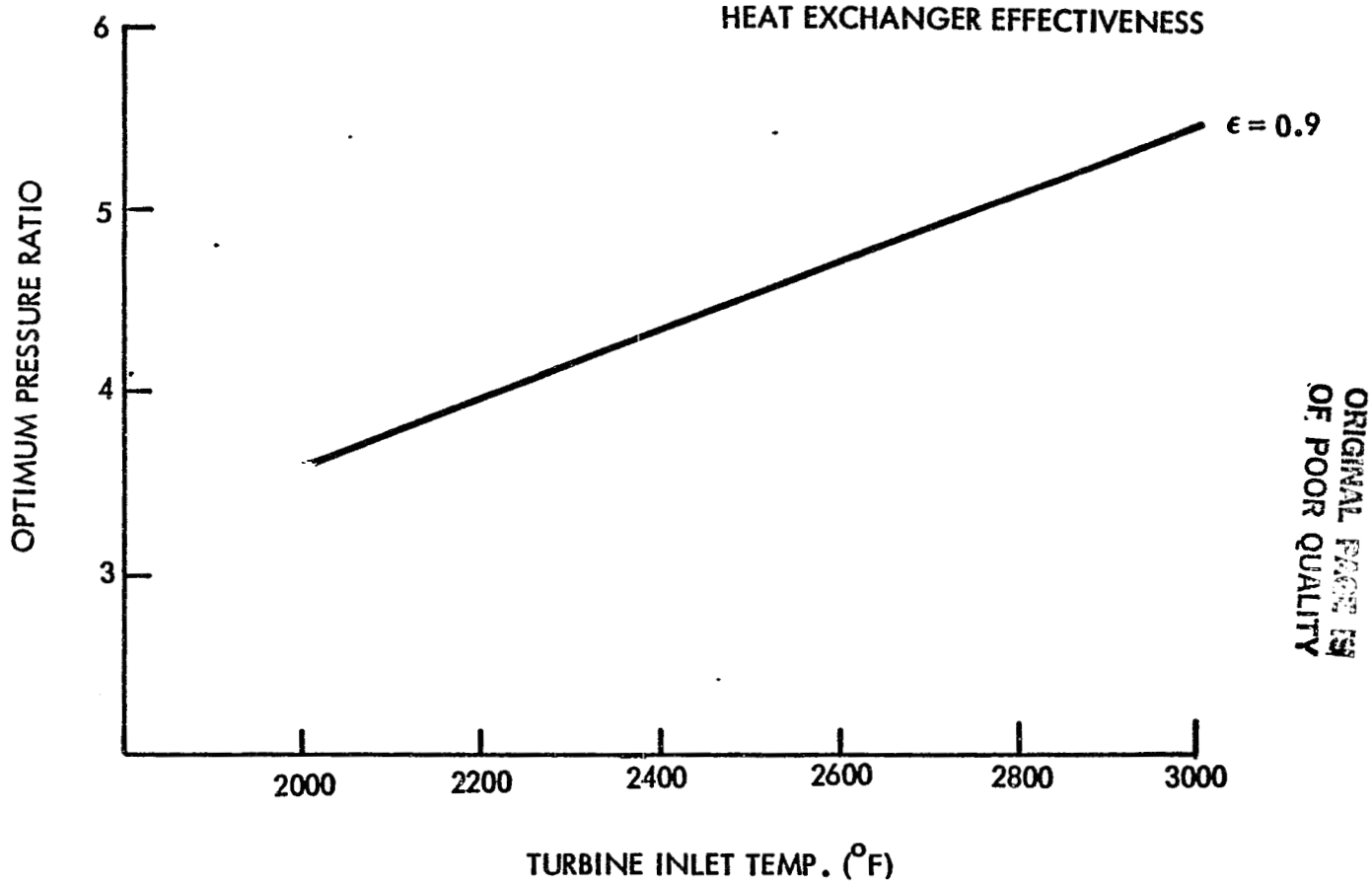

ORIGINAL PAGE IS
OF POOR QUALITY

Figure 5. Optimum Pressure Ratio versus Turbine Inlet Temperature

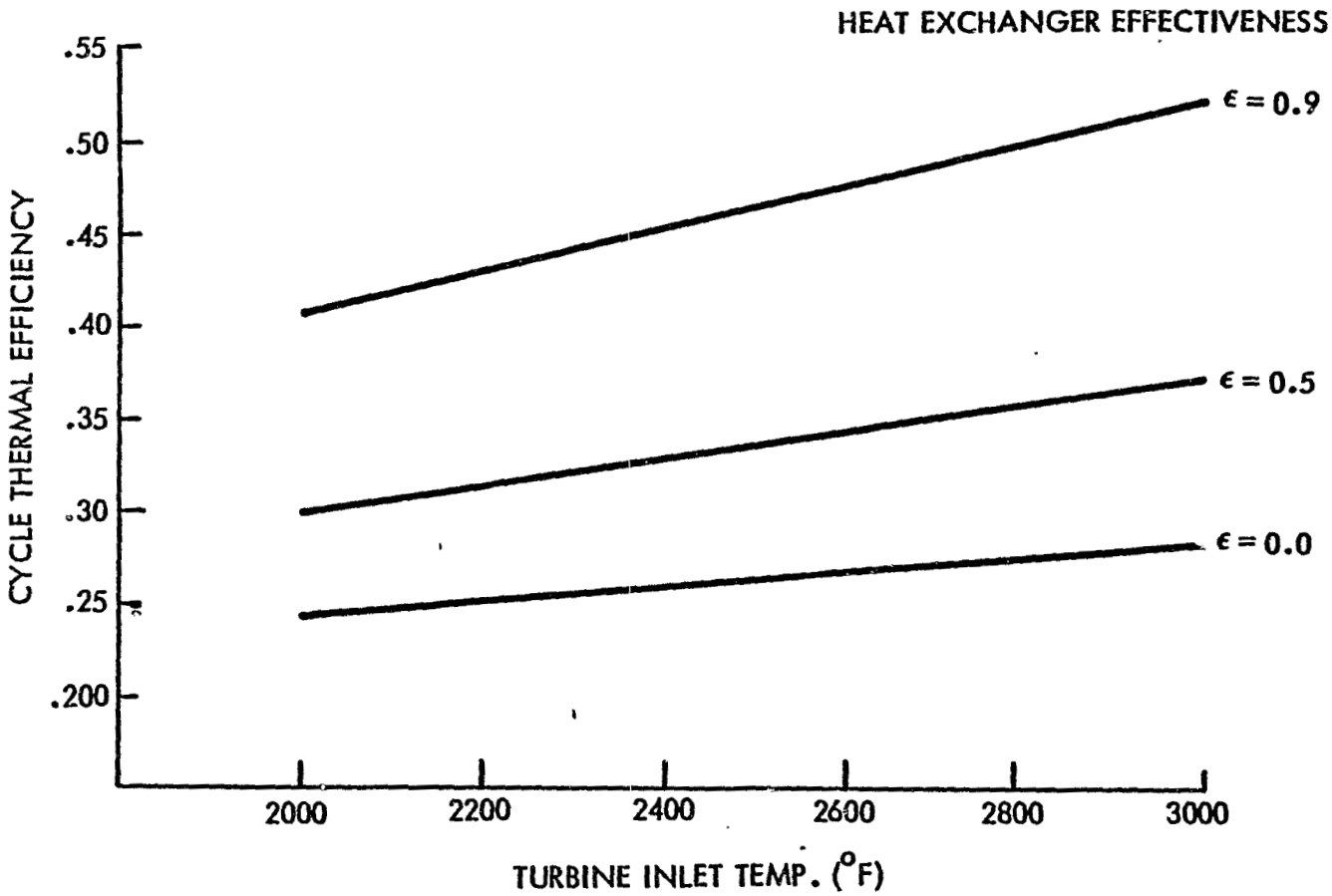

ORIGINAL PAGE IS
OF POOR QUALITY

Figure 6. Cycle Efficiency at the Optimum Pressure Ratio versus Turbine Inlet Temperature

recuperating to 90%, a 100% efficiency improvement is obtained at any temperature between 2000 to 3000°F range. The limited use of metalic recuperators above 1500°F suggests the use of ceramic storage modules on heat exchangers that could be capable of operation to 3000°F with 90% effectiveness.

The receiver inlet temperatures were a byproduct of the cycle analyses. In Figure 7 the receiver inlet temperature rises with turbine inlet temperature at the optimum pressure ratio. This is clear when refering to the T-S diagram where point 2" would move to higher temperatures as turbine inlet temperatures are increased. This effect is most pronounced with the highest recuperated engine. In effect, raising turbine inlet temperatures also raises the mean temperature during heat addition in recuperated engines whereas in unrecuperated ones, the receiver inlet temperature, basically corresponds to the compressor outlet temperature.

Figure 8 shows receiver inlet temperatures as a function of turbine inlet temperature and pressure ratio for a recuperator effectiveness of 0.9. The dashed curve shows the optimum pressure ratio, r_p, and Turbine Inlet Temperatures, TIT.

The window cooling limit, discussed in a following section has been added to this figure to show the engine operating restrictions imposed by the window cooling requirement.

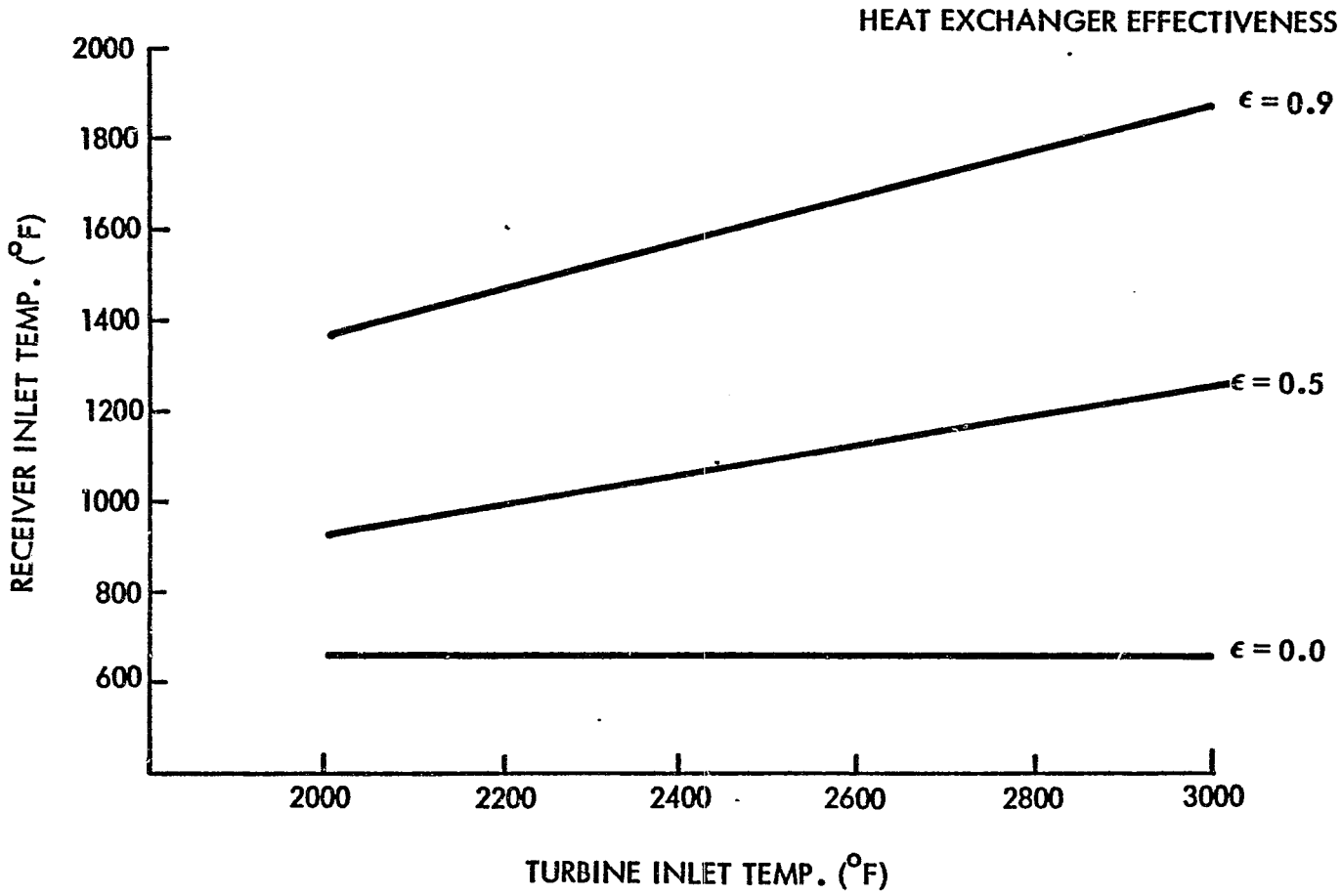

Figure 7. Receiver Inlet Temperature At the Optimum Pressure Ratio versus Turbine Inlet Temperature

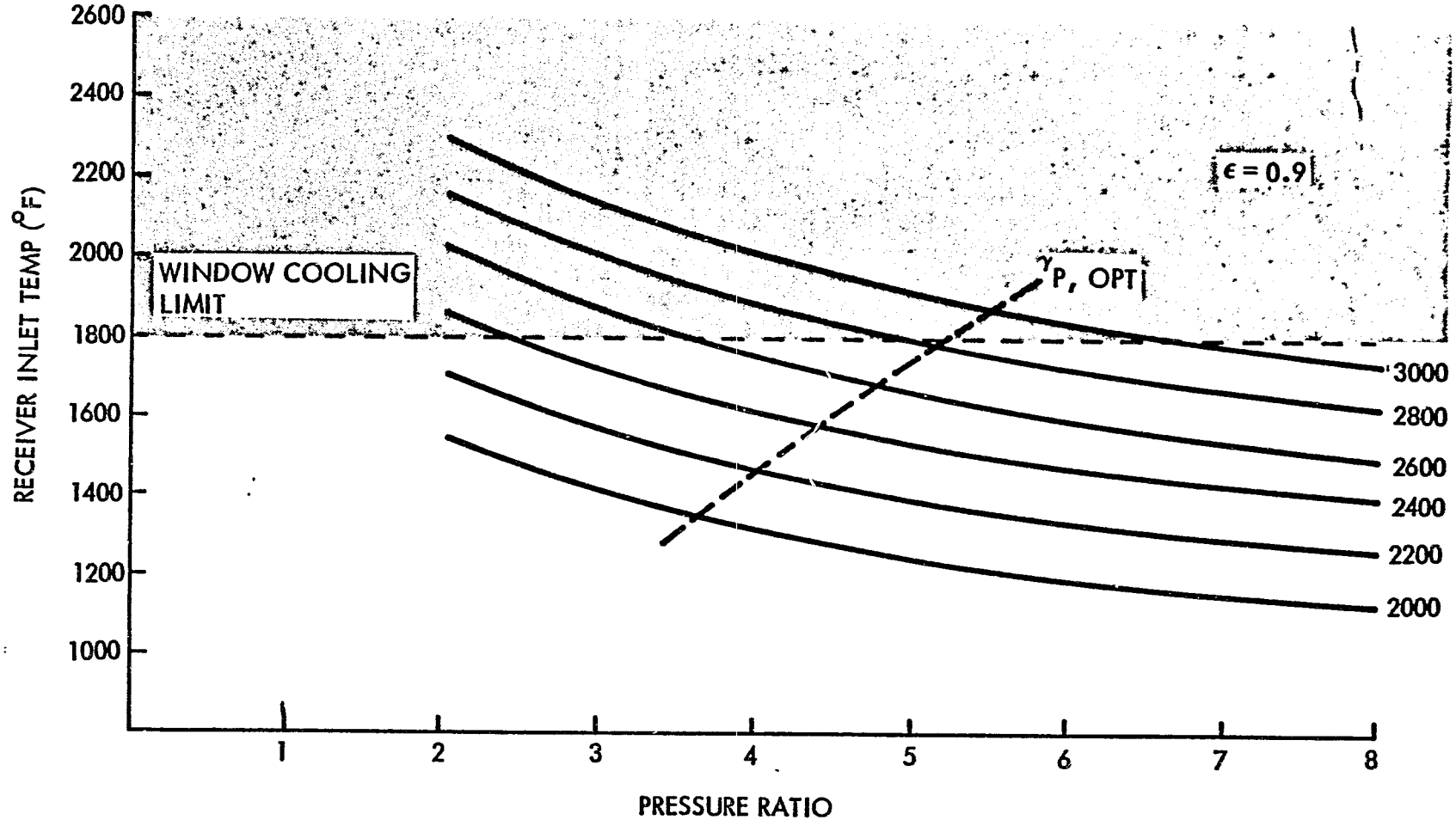

Figure 8. Receiver Inlet Temperature versus Pressure Ratio and Turbine Inlet Temperature

ORIGINAL PAGE IS
OF POOR QUALITY

DESIGN POINT

A representative design point was selected as a baseline in order to optimize the parametric analysis task. The design point selected was nominally 75 kw, because it coincides with the collector capabilities cited in Exhibit I of the contract. Off design trends were noted and are identified. Performance parameters were calculated for alternate power levels throughout the specified range.

APERTURE SIZING

Work done during preparation of the Sanders proposal suggested significant reduction in radiation losses would be realized through the use of an advanced terminal concentrator. Therefore, prior to starting the flux modeling effort the existing computer model, FLUXGO, was modified to accommodate the more complex terminal concentrator which is commonly referred to as the Winston Cone. The modified program, dubbed CPCFLUX, was used to evaluate the performance of the baseline receiver as its geometric and optical properties were varied.

The following parameters were used to describe the baseline receiver/collector set as shown in Table 3 below. Figure 9, following the baseline design table serves to pictorially define the input parameters.

The cavity aperture was ranged from 11.8 to 21.8 cm diameter. CPCFLUX results provide data points to derive the quartic polynomial:

$$P = 4.26E4 + 3.445E2a - 1.731A^2 + 4.369E\text{-}3a^3 - 4.28E\text{-}6a^4$$

where P is captured power (watts) and a is aperture area (cm^2).

Radiative losses from the cavity are a function of cavity size and temperature with an assumed emissivity of 1.0.

TABLE 3. CPC FLUX: INPUT DESCRIPTORS

Name	Description	Baseline Value English	Baseline Value Metric
REFRAD	Radius of the primary collector	217"	5.51m
REFOCAL	Focal length of primary collector	260.4"	6.61m
RVRTXZ	Distance from cavity aperture and primary collector vertex		6.83m
RREFL	Reflectivity of primary collector		0.92
RSIGMA	Standard surface slope error of primary collector, radians		0.002
RBLANK	Center shadow radius on primary collector	21.0"	0.533m
SUNFLX	Solar insolation constant, watts-m^{-2}		1000
SUNSIZ	Angular semidiameter of the (gaussian) sun, radians		0.0044
RTHROT	Radius of CPC exit aperture (the small end)	3.29"	0.084m
THETA	Maximum off axis acceptance angle of CPC, radians		0.75
CPCREF	Reflectivity of the CPC		0.92
CPCSIG	Standard surface slope error of the CPC, radians		0.001
ZMAX	Length of the CPC, separation of entrance and exit planes		0.221m
NRAY	Number of rays in sample	(typically)	20,000
CAVRAD	Cavity radius, of cylindrical vertical wall		0.300
CAVHGT	Cavity height, distance from aperture to flat circular roof	18.0"	0.457
CAVABS	Cavity wall absorptivity		1.00

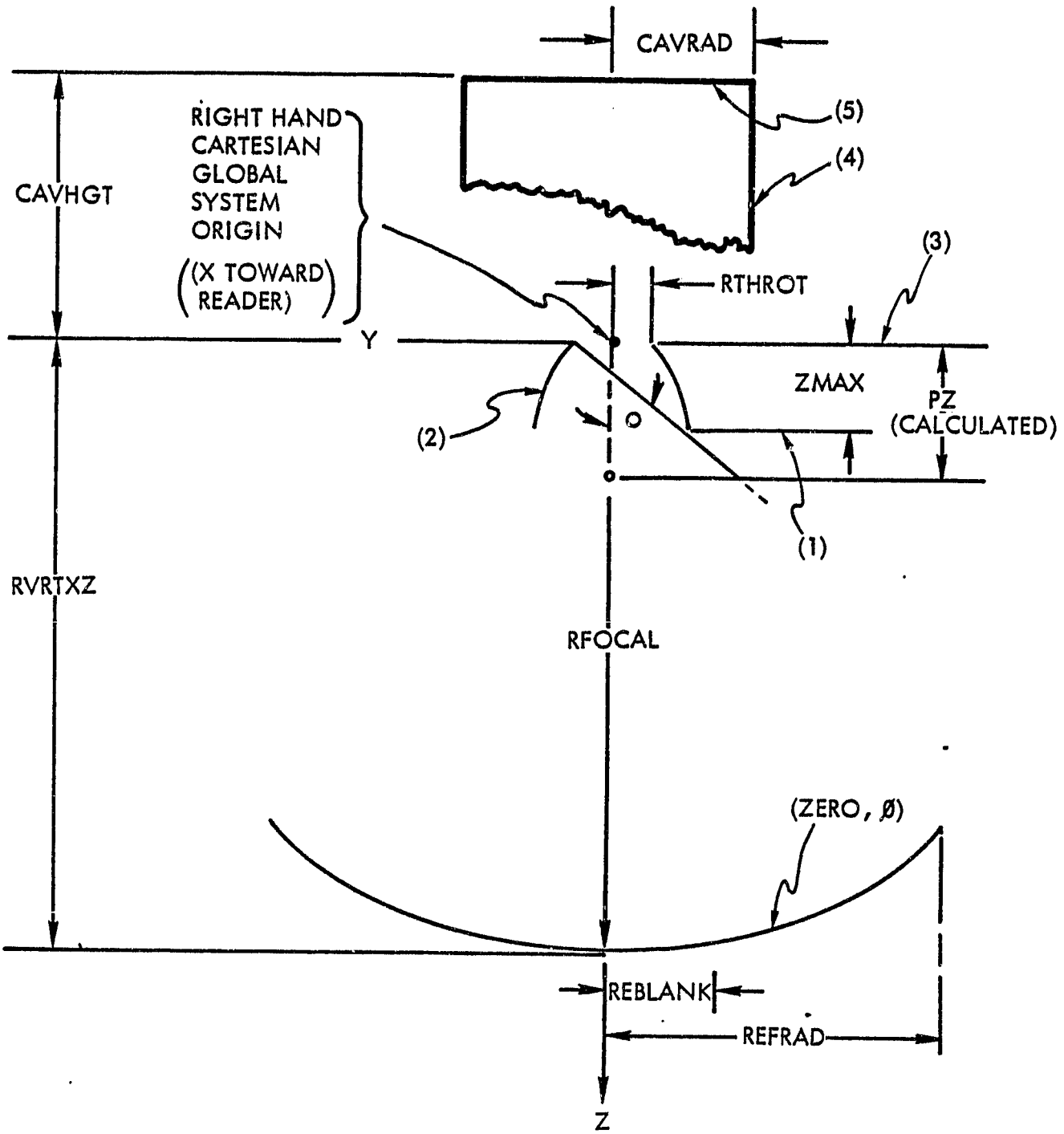
CAVRAD
CAVHGT
RIGHT HAND
CARTESIAN
GLOBAL
SYSTEM
ORIGIN
(X TOWARD
READER)
(5)
(4)
(3)
RTHROT
Y
ZMAX
PZ
(CALCULATED)
(2)
O
(1)
RVRTXZ
RFOCAL
(ZERO, Ø)
REBLANK
REFRAD
Z

Figure 9.

Then for each cavity temperature radiative losses are a linear function of area. Optimum aperture size can then be selected as that size at which net power is maximized. Figure 10 below shows the results of these tradeoffs, without a window. The figure can be used as a design guide; at 2400^{o} cavity temperature optimum aperture area is 215 cm^{2} and net power is 64 kw.

A windowed aperture admits less light due to reflection and mitigates reradiation. These factors lead to a different aperture size if net power is to be maximized. These findings are graphed in Figure 11.

The results of aperture size optimization are tabulated below as a function of cavity temperature with the baseline system.

Temperature ^{o}F	Open Aperture Power	Open Aperture Area-cm^{2}	Windowed Aperture Power	Windowed Aperture Area-cm^{2}
2000	67.5 kw	314	63.8 kw	331
2200	65.5	285	62.1	313
2400	63.2	215	59.7	265
2600	61.1	178	57.5	200
2800	58.8	152	55.3	165
3000	56.6	132	53.0	141

Conversion efficiency is given below for the baseline, 70 kw receiver/CPC combination with and without window as a function of temperature. Efficiency is defined as power in (delivered to cavity entrance aperture) less reradiated power lost divided by power in.

$$\eta = \frac{P_{in} - P_{loss}}{P_{in}} = 1 - \frac{P_{loss}}{P_{in}}$$

ORIGINAL PAGE IS
OF POOR QUALITY

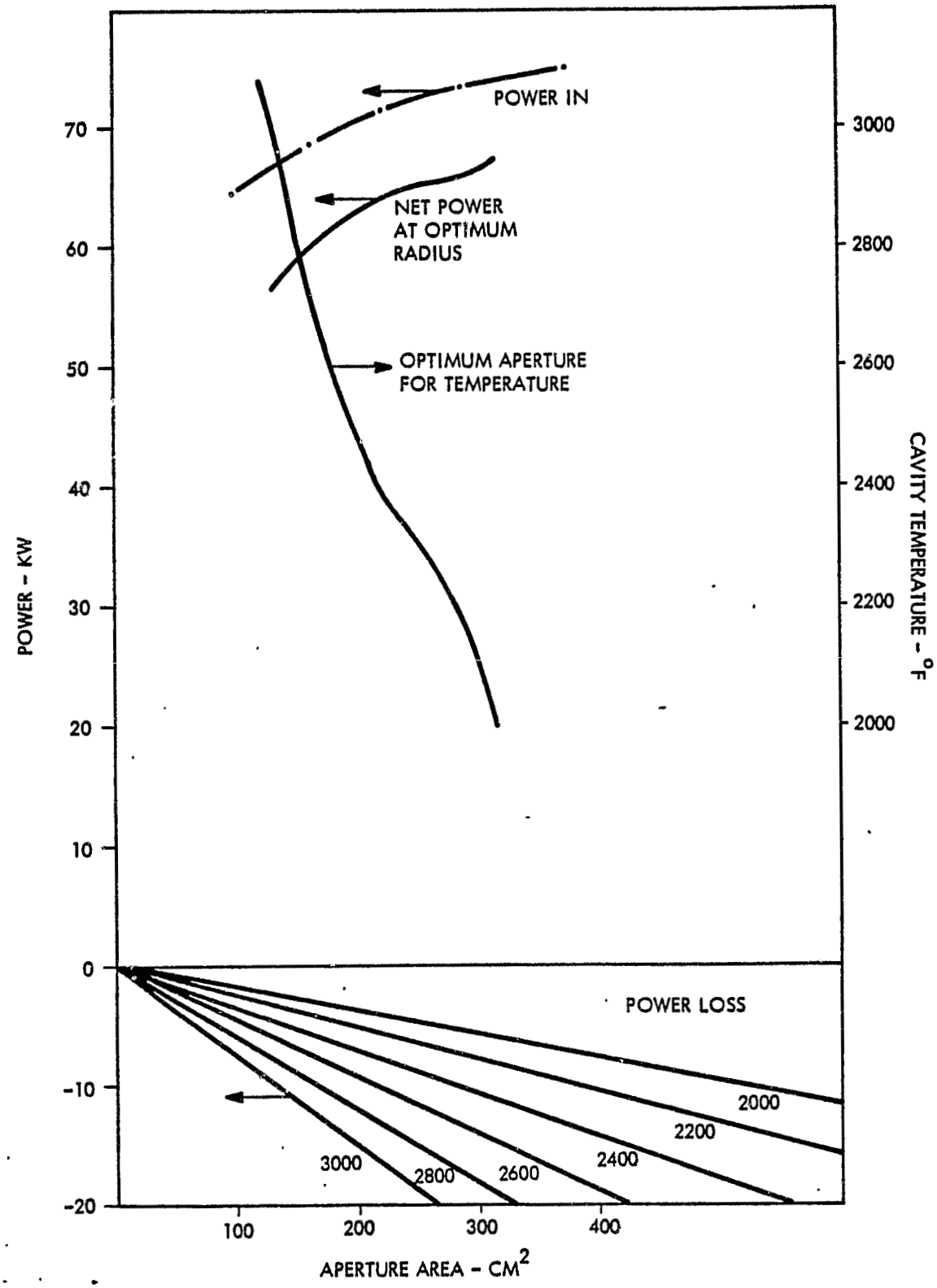

Figure 10. Open Receiver

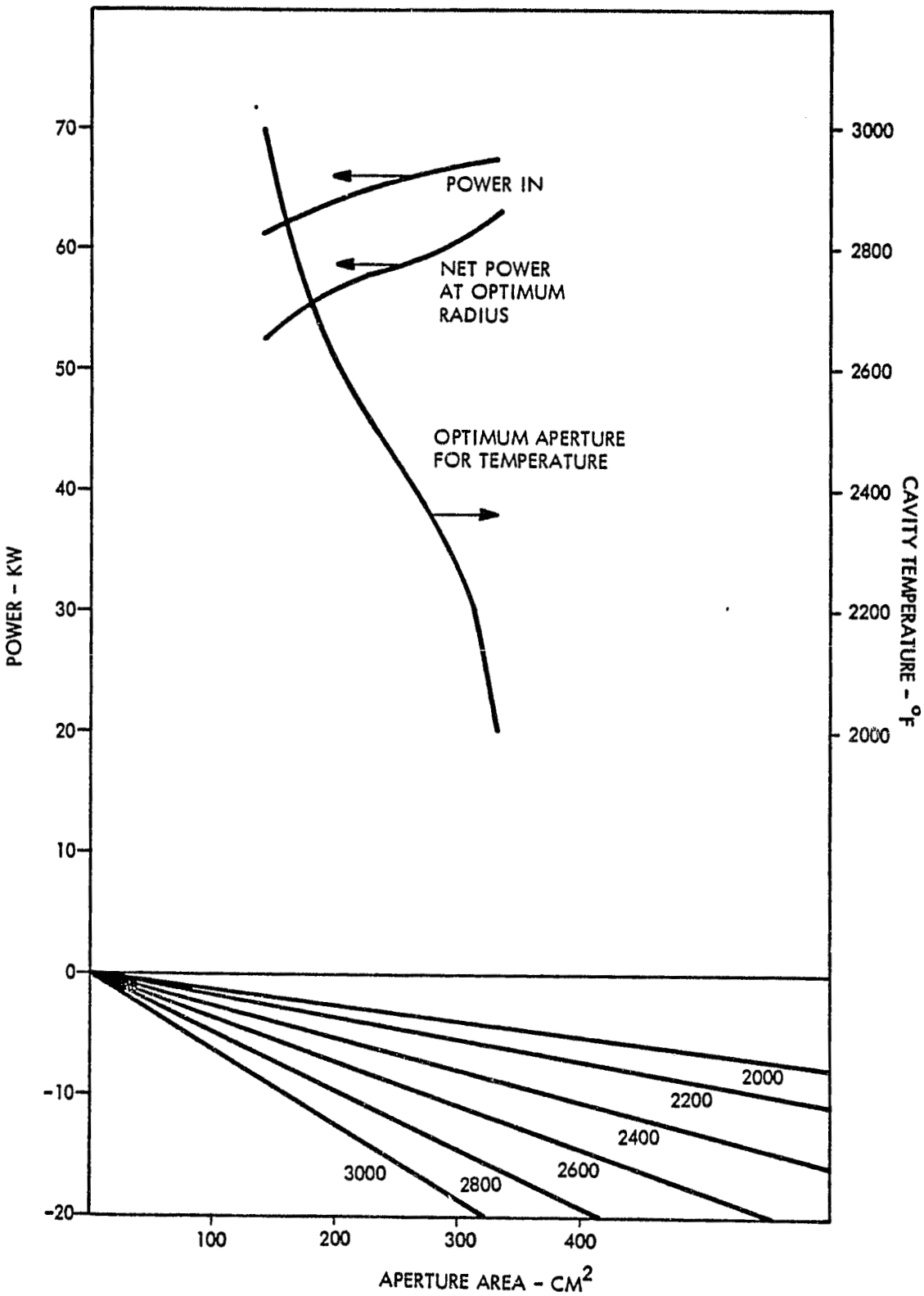

Figure 11. Windowed Receiver

	CAVITY EFFICIENCY	
Temperature	Open Aperture	Windowed
2000	0.912	93.7
2200	0.896	91.5
2400	0.891	89.5
2600	0.880	88.9
2800	0.864	87.4
3000	0.849	85.6

FOCAL POINT LOCATION

The impact of moving the focal point above and below the entrance aperture plane of the terminal concentrator (CPC) was investigated to find the optimum position. The optimum position was shown to be with the aim-point 1.0 to 2.0 cm within the CPC entrance plane and on axis. With optimum placement and 92% CPC reflectivity light from the collector (11 meter primary mirror) is distributed as follows:

Direct input through aperture	24.0%
Redirected by CPC into aperture	58.0%
TOTAL CAPTURE	82.0%
Rejected by CPC	8.5%
Absorbed on CPC	7.0%
Miss CPC	2.5%
	18.0%
TOTAL REFLECTED BY PRIMARY	100%

These performance calculations are shown in Figures 12A and B.

POWER SCALING

The receiver/collector set was scaled over a power range from 15 to 500 kw. The results of that scaling are given below. It is noteworthy that the average flux was 300 watts cm^{-2} at the cavity entrance aperture and the maximum flux near the center was about 1.3 kw cm^{-2}.

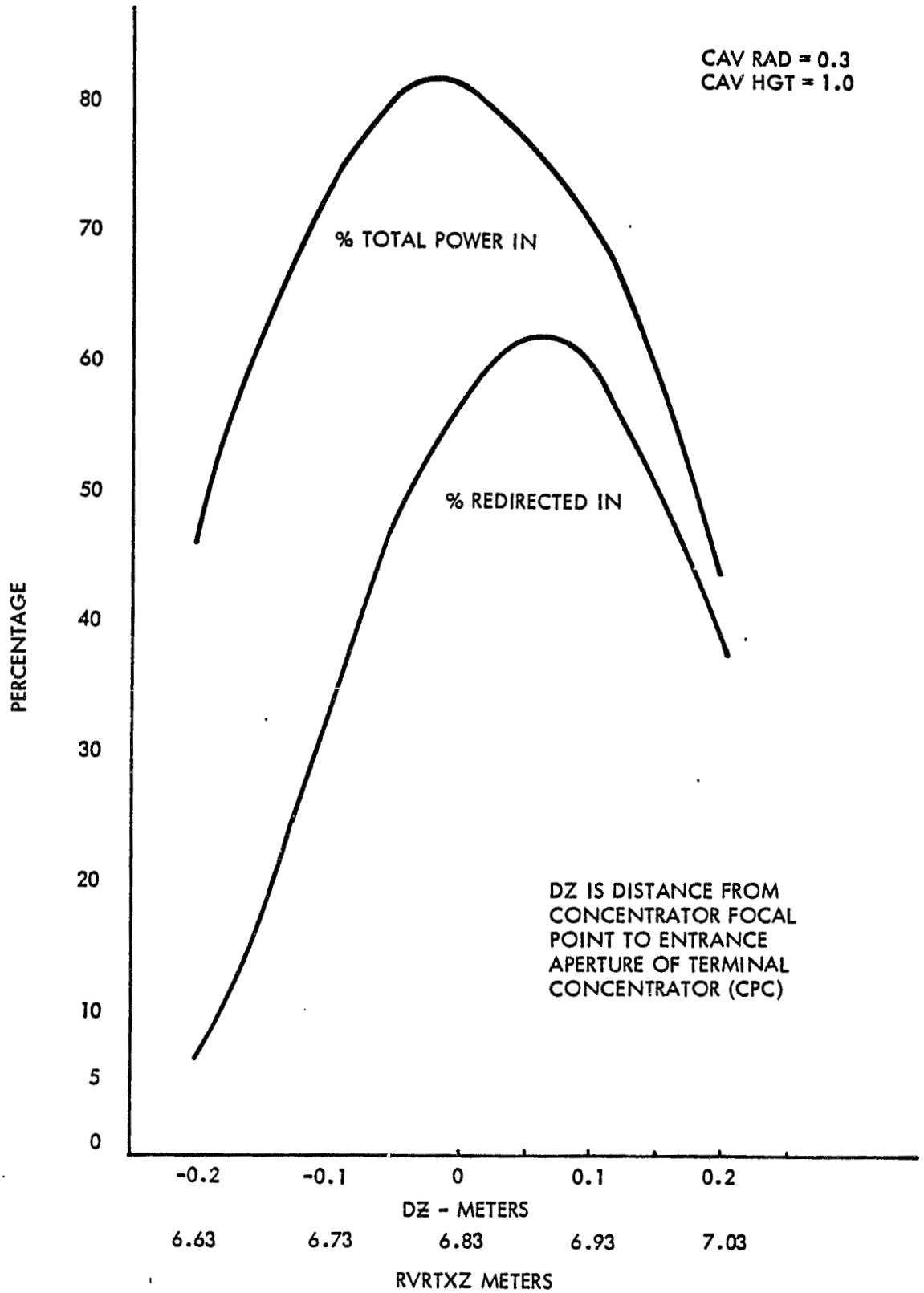

Figure 12A. Energy Distribution

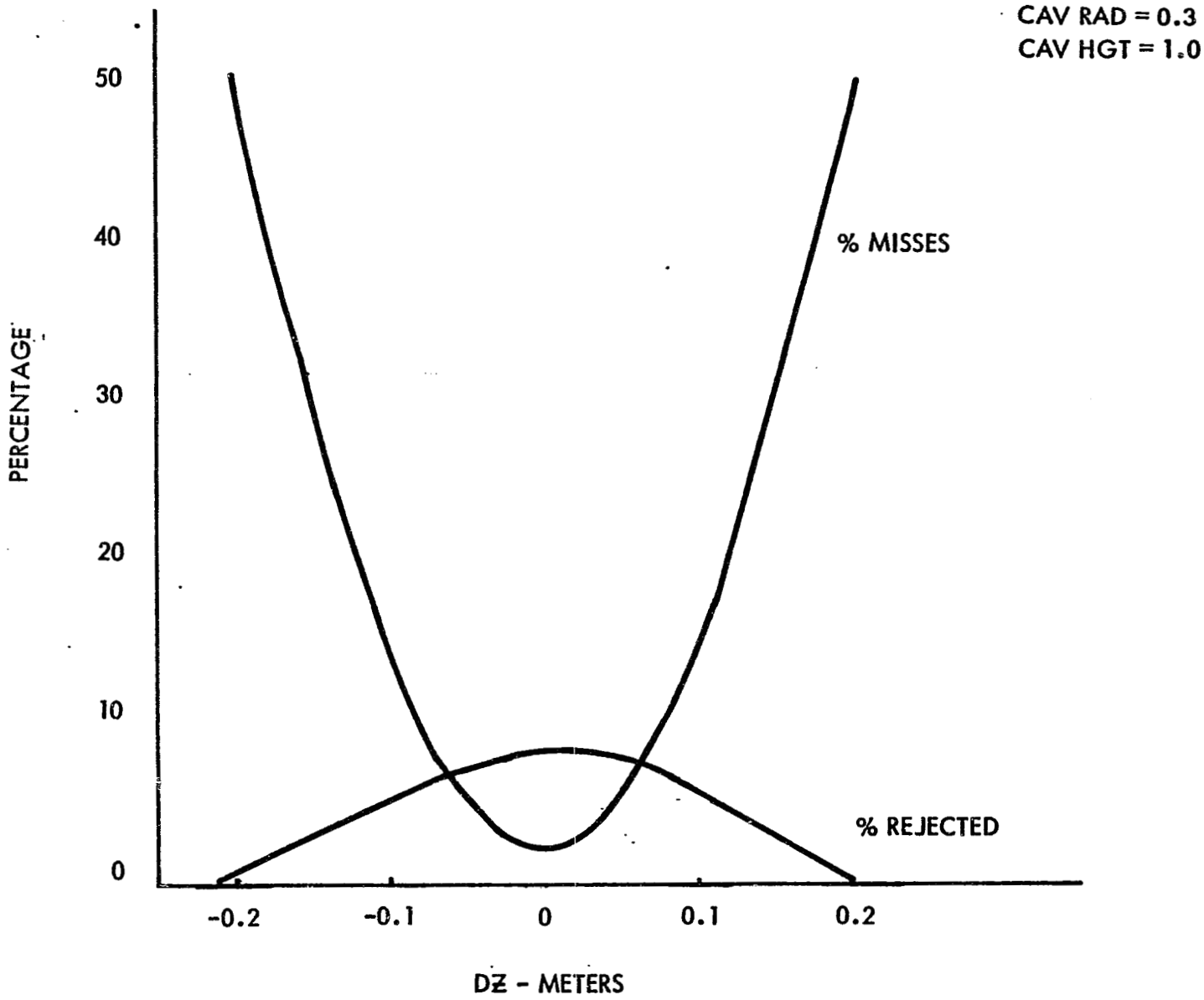

Figure 12B. Energy Distribution

Collector Diameter meters	Power Captured k-watts	Peak Flux watts cm^{-2}	Average Flux watts cm^{-2}
5.1	15.2	1300	319
7.5	33.0	1300	324
11.0	71.3	1350	324
15.0	132.0	1300	322
17.8	187.0	1300	321
28.8	489.0	1250	321

These results are given graphically in Figure 13.

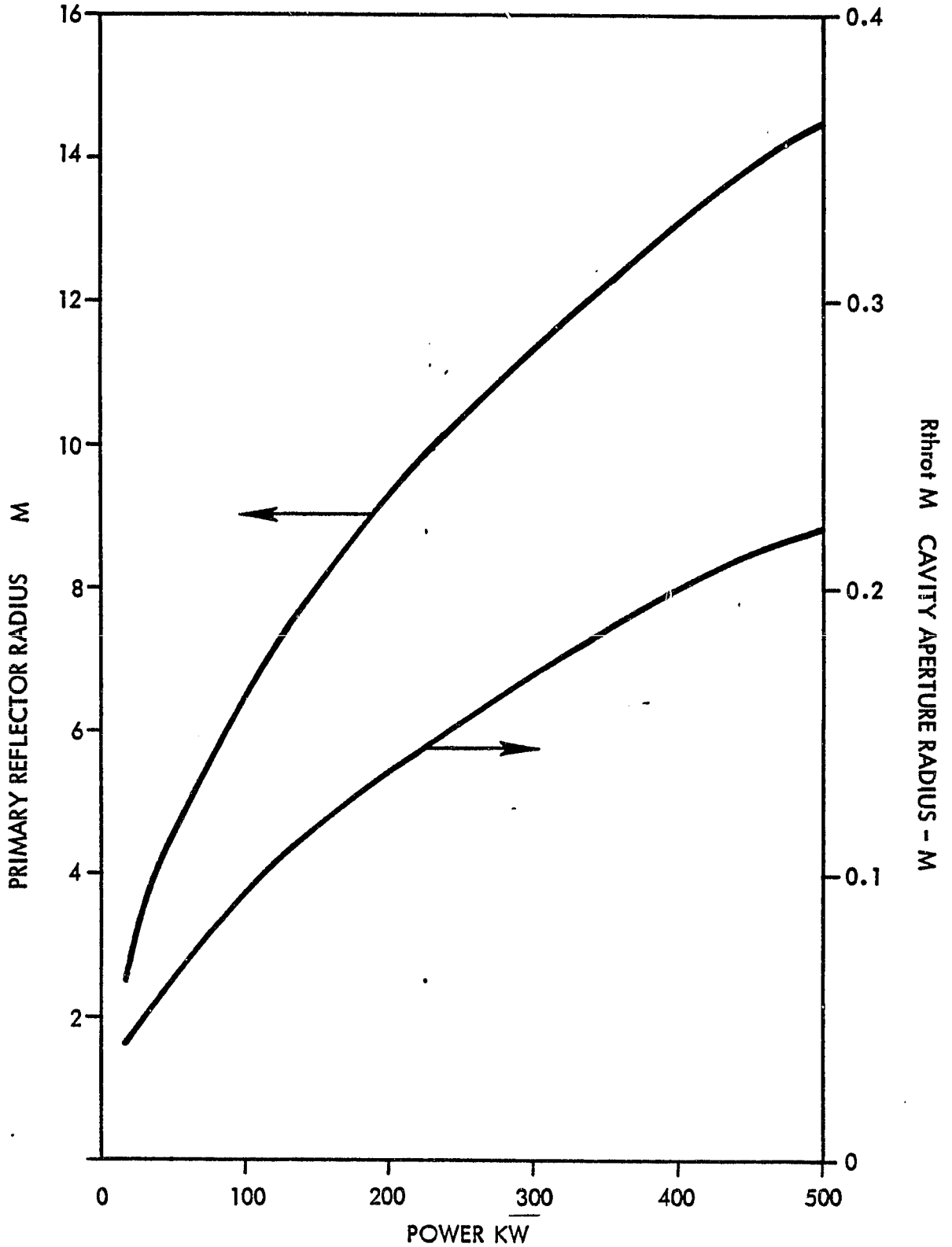
16
14
12
10
8
6
4
2
0.4
0.3
0.2
0.1
0
0
100
200
300
400
500
POWER KW
PRIMARY REFLECTOR RADIUS M
Rthrot M CAVITY APERTURE RADIUS - M

Figure 13.

FLUX DISTRIBUTION

The determination of flux distributions at and behind the aperture is vital to selection of a viable design. The flux at the aperture of course has direct bearing on the window temperature rise. Behind the aperture, placement of active heat transfer surfaces in regions of moderately dispersed flux is important to the survival of materials and the lowering of peak cavity temperatures.

Numerical evaluation of these fluxes is accomplished by a Monte Carlo method of tracing a sifficiently large sample of random generated rays through the system optics to achieve a physically meaningful distribution.

A step by step synopsis of the program is given below.

CPCFLUX

1. Read input parameters
2. Generate random ray
3. Aim at focal point
4. Deviate according to collector surface quality
5. Project to CPC entrance aperture
6. Test for miss
7. Test for direct entrance
8. Test for intercept on CPC
9. Test for reflection/absorption
10. Redirect consistent with CPC surface quality
11. Test for outward reflection
12. Test for cavity entrance or multiple bounce on CPC
13. Enter cavity
14. Impinge on wall or roof
15. Record significant events
16. Return to 1 until ray sample is complete
17. Print results

The baseline design for the analysis has been a 70 kw receiver. The CPC used in the model has the dimensions shown in Figure 14. It effectively directs rays within the maximum acceptance angle into the cavity and sharply rejects those rays originating outside the specified acceptance cone. Transition from acceptance to rejection occurs over a range of about (<2 degrees) 0.03 radians in a three dimensional CPC surface of revolution.

Compilation of the results of 21 CPCFLUX samples provides the magnitude of vertical and radial flux components as a function of radius and distance behind the aperture of the baseline receiver/collector set. These components may be vectorially added to yield total flux magnitudes and directions. Tables 4, 5, and 6 show these respective values. The tabulated data is presented in the form of cross-section views of volume contours on Figures 15, 16 and 17.

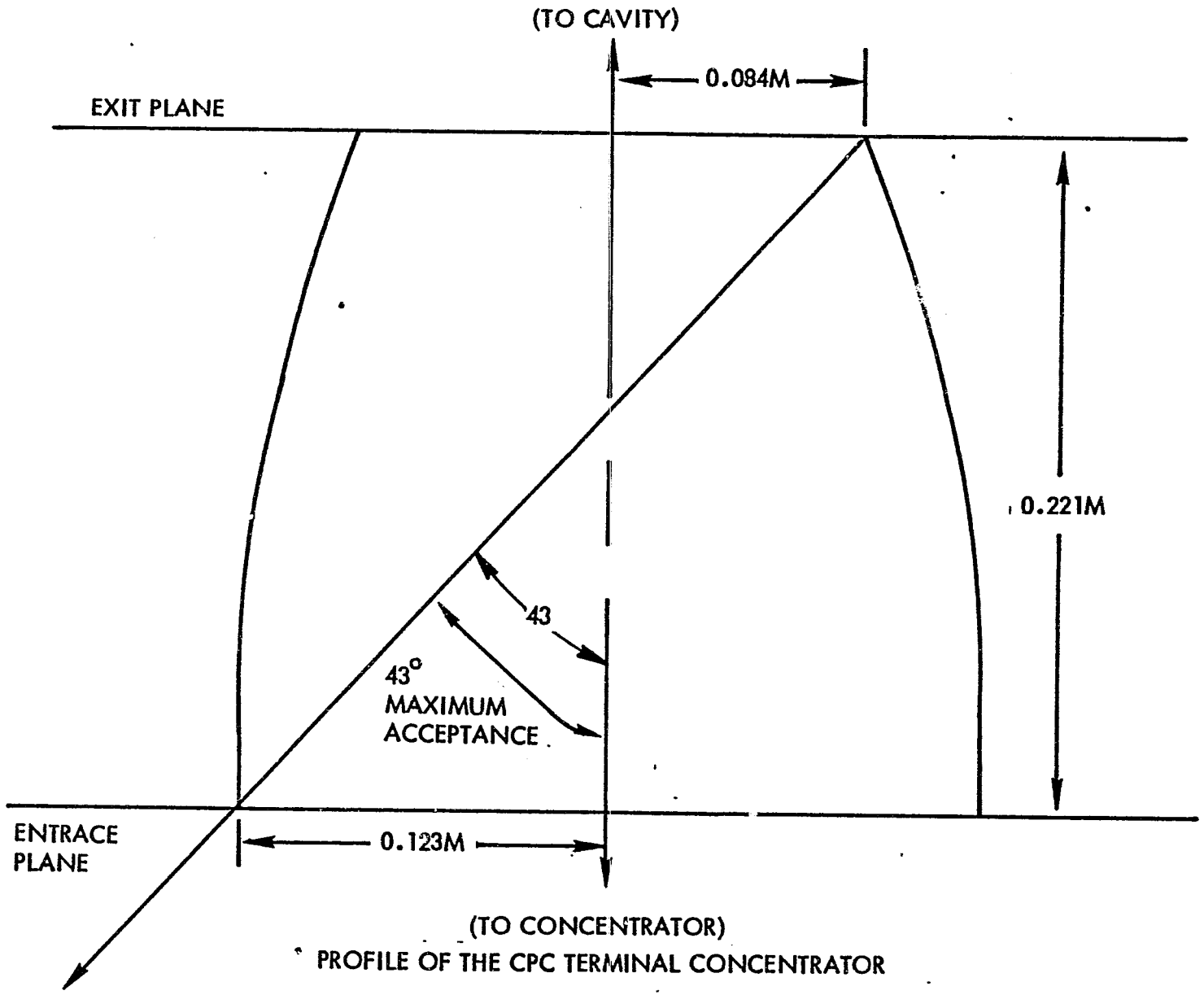

PROFILE OF THE CPC TERMINAL CONCENTRATOR

Figure 14.

TABLE 4. VERTICAL FLUX COMPONENT COMPILATION - $W \cdot cm^{-2}$

HEIGHT - m	0.1	0.2	0.3	0.4	0.5	0.6	0.7	0.8	0.9	1.0
1.0	1.38	2.59	2.40	2.02	1.33	0.85	0.53	0.35	0.32	0.34
0.9	1.81	3.08	2.86	2.08	1.32	0.79	0.49	0.42	0.41	0.46
0.8	2.59	3.77	3.33	2.15	1.28	0.72	0.54	0.53	0.56	0.58
0.7	3.39	4.68	3.77	2.25	1.23	0.74	0.70	0.75	0.75	0.73
0.6	4.98	5.67	4.29	2.21	1.22	0.93	0.98	1.07	0.93	0.87
0.5	7.07	7.43	4.50	2.15	1.41	1.41	1.51	1.30	1.07	0.80
0.4	1.02	9.35	4.81	2.44	2.20	2.15	1.87	1.33	0.88	0.57
0.3	15.31	12.12	5.37	3.86	3.67	2.48	1.46	0.82	0.44	0.28
0.2	26.02	16.80	8.56	6.28	3.00	1.28	0.62	0.31	0.15	0.09
0.1	59.64	31.54	9.51	2.13	0.51	0.18	0.09	0.01	0.01	0.01
0.05	131.62	27.32	1.93	0.28	0.09	0.03	0.02	0.0	0.0	0.0

RADIUS - m

TABLE 5. RADIAL FLUX COMPONENT COMPILATION - $W \cdot cm^{-2}$

HEIGHT - m	0.1	0.2	0.3	0.4	0.5	0.6	0.7	0.8	0.9	1.0
1.0	0.167	0.486	0.605	0.551	0.424	0.397	0.246	0.271	0.318	0.369
0.9	0.403	0.625	0.909	0.738	0.530	0.410	0.355	0.372	0.458	0.523
0.8	0.403	0.838	0.974	0.702	0.548	0.478	0.486	0.548	0.687	0.823
0.7	0.693	1.080	1.355	0.834	0.596	0.647	0.763	0.904	1.065	1.120
0.6	0.941	1.820	1.353	0.980	0.814	1.060	1.320	1.400	1.514	1.260
0.5	1.400	2.202	1.610	1.310	1.630	2.100	2.100	1.960	1.680	1.310
0.4	2.350	3.030	2.320	2.540	2.340	3.440	2.520	1.990	1.440	0.954
0.3	4.180	3.860	4.850	6.300	5.240	3.580	2.240	1.380	1.010	0.679
0.2	9.540	12.770	13.670	7.940	3.900	2.160	1.160	0.635	0.383	0.270
0.1	71.980	29.650	7.090	2.090	0.878	0.485	0.283	0.200	0.145	0.09
0.05	95.48	6.770	1.330	0.505	0.254	0.137	0.080	0.653	0.033	0.028

RADIUS - m

TABLE 6. TOTAL FLUX COMPILATION - $W \cdot cm^{-2}$ AND ELEVATION - DEGREES

HEIGHT - m	0.1	0.2	0.3	0.4	0.5	0.6	0.7	0.8	0.9	1.0
1.0	1.39	2.64	2.48	2.09	1.40	0.94	0.58	0.44	0.45	0.50
	83.10	79.37	75.85	74.74	72.32	64.97	65.10	52.25	45.18	42.66
0.9	1.85	3.14	3.00	3.21	1.42	0.89	0.36	0.56	0.62	0.70
	77.45	78.53	72.37	40.47	68.12	62.57	7.86	48.47	41.84	41.33
0.8	2.62	3.86	3.47	2.26	1.39	0.86	0.73	0.79	0.89	1.01
	81.16	77.47	73.70	71.92	66.82	56.42	48.01	42.39	39.19	35.17
0.7	3.46	4.80	4.01	2.40	1.37	0.98	1.04	1.18	1.39	1.34
	78.45	77.01	70.23	69.66	64.15	48.84	42.53	39.68	35.15	33.10
0.6	5.07	5.96	4.50	2.42	1.47	1.41	1.64	1.76	1.78	1.53
	79.30	72.20	72.50	66.09	56.29	41.26	36.59	37.39	31.56	34.62
0.5	7.21	7.70	4.78	2.52	2.16	2.53	2.59	2.35	1.99	1.54
	78.80	74.79	70.31	58.65	40.86	33.88	35.72	33.56	32.49	31.41
0.4	10.47	9.83	5.34	3.52	4.0	4.06	3.14	2.39	1.69	1.11
	77.03	72.04	64.25	43.85	33.37	32.01	36.58	33.76	31.43	30.86
0.3	15.87	13.06	7.24	7.39	6.40	4.24	2.67	1.61	1.10	0.73
	74.73	68.15	47.91	31.50	35.01	35.79	33.10	30.72	23.54	22.41
0.2	27.71	21.10	16.13	10.12	4.92	2.511	1.32	0.71	0.41	0.29
	69.87	52.76	32.05	38.34	37.57	30.65	28.12	26.02	21.39	18.44
0.1	93.48	48.29	11.86	2.98	1.02	0.517	0.30	0.20	0.15	0.91
	39.64	46.77	53.29	45.54	30.15	20.36	17.64	2.86	3.95	0.63
0.05	162.61	28.15	2.34	0.577	0.27	0.14	0.08	0.65	0.33	0.28
	54.04	76.08	55.43	29.01	19.51	12.35	14.04	0.0	0.0	0.0

RADIUS - m

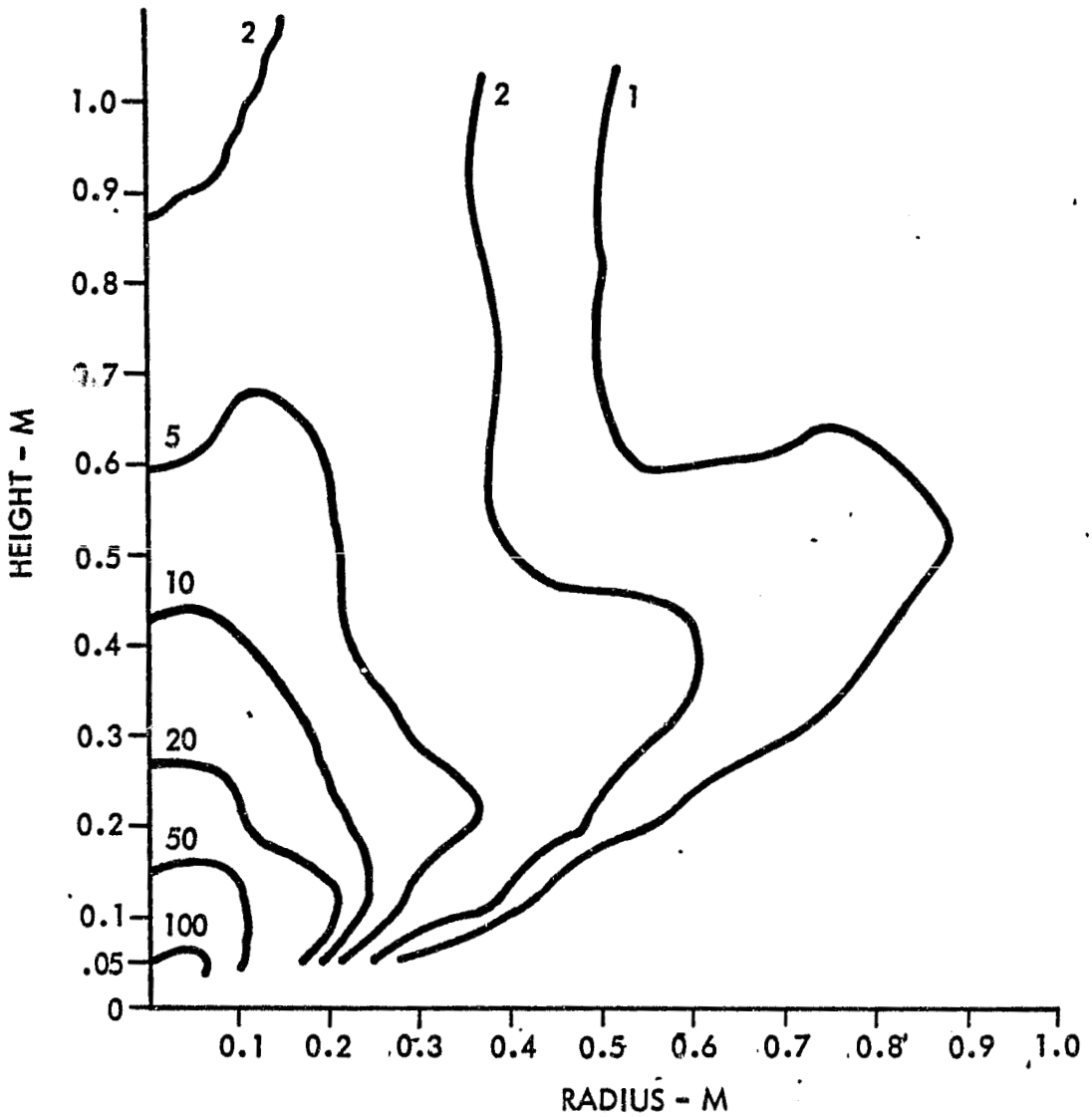

Figure 15. Vertical Flux Component versus Position $W \cdot cm^{-2}$

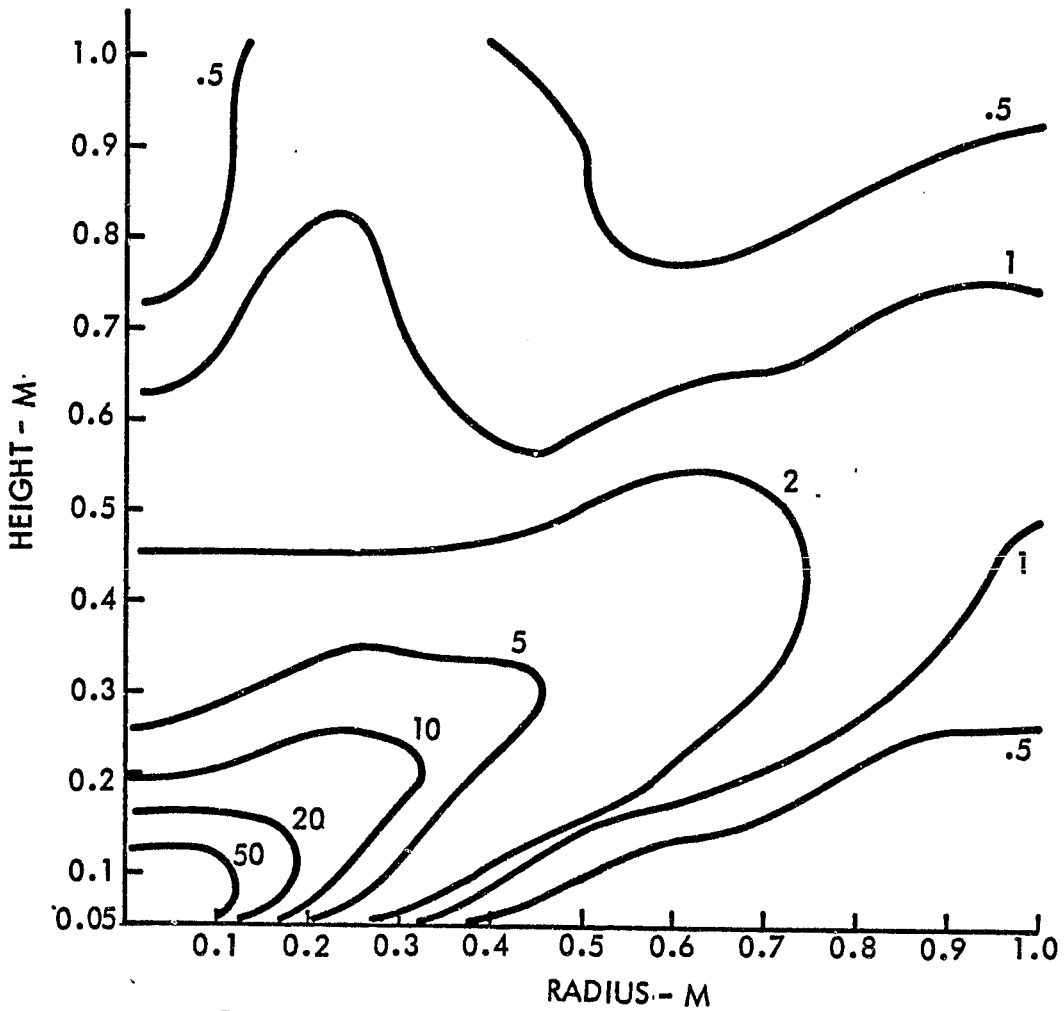

Figure 16. Radial Flux Component versus Position
$W \cdot cm^{-2}$

TOTAL

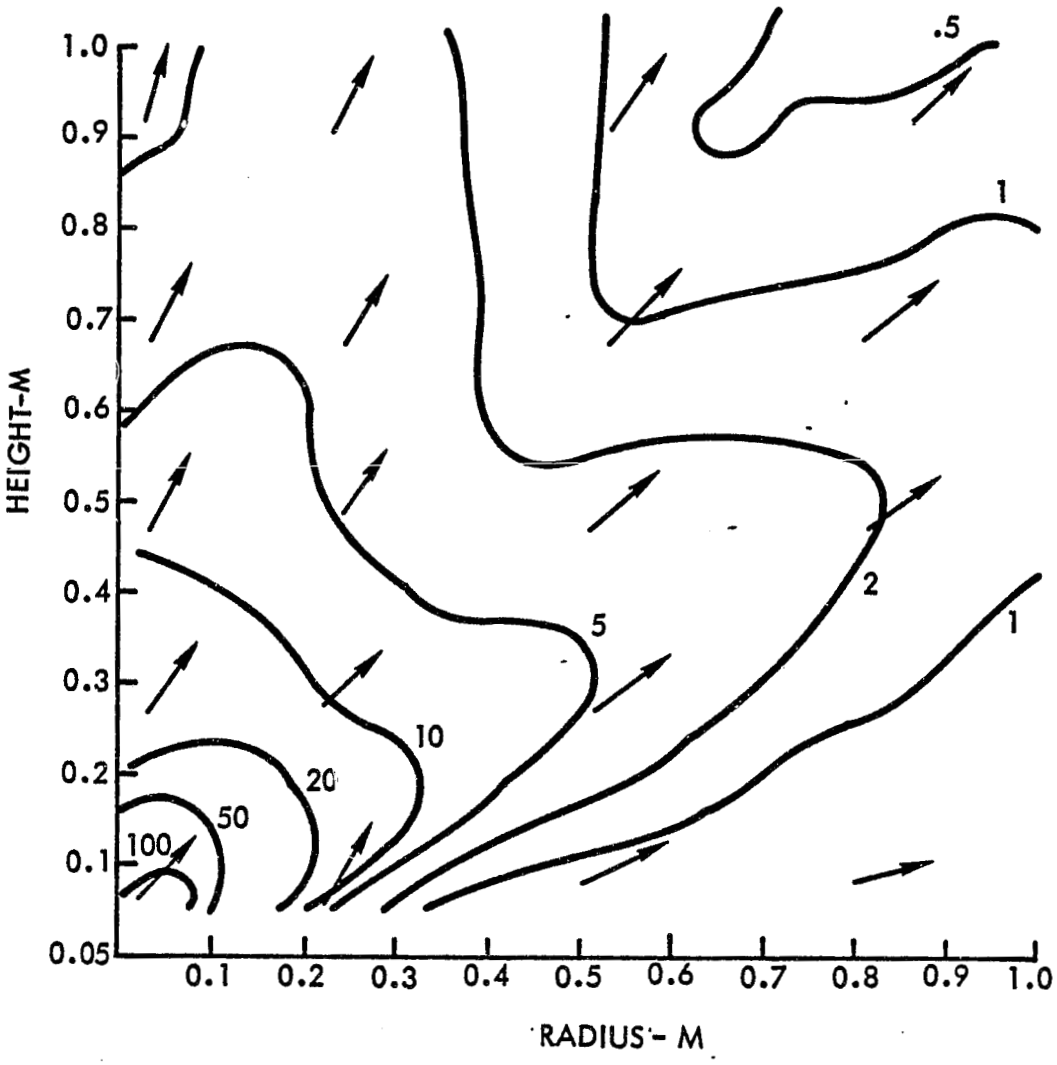

Figure 17. Total Flux versus Position $W \cdot cm^{-2}$

WINDOW HEAT LOAD

Flux passing through the aperture window heats the window by the process of distributed absorption. The distributed heating is calculated as follows:

Frontal flux is F_T, the amount of energy following within a given spectral bandwidth is:

$$F_{\Delta\lambda} = F_T \times f_{\Delta\lambda}$$

The flux at any depth χ may be described as

$$F_\chi = F_{\Delta\lambda} \cdot e^{-\alpha\chi}$$

The absorbed power is then

$$F_{\Delta\lambda_A} = F_{\Delta\lambda_0} - F_{\Delta\lambda_\chi}$$

in every band of interest.

The power being conducted back toward the front surface as a function of depth, χ, is equal the difference between the absorbed power at the adiabatic plane (rear surface) and the absorbed power at depth, χ.

$$\dot{q}_\chi = F_{\Delta\lambda_\chi} - F_{\Delta\lambda_a}$$

Because the temperature gradient may be expressed $dT = \frac{1}{kA} d(\dot{q}_\chi \chi)$.

Then the temperature gradient can be calculated from the integral:

$$\Delta T = \frac{F_{\Delta\lambda}}{k} \int_0^a (e^{-\alpha\chi} - e^{-\alpha a})$$

Evaluating across the full window thickness, a, the expression becomes:

$$\Delta T = \frac{F_{\Delta\lambda}}{k} \left(\frac{1}{\alpha} - \left(a + \frac{1}{\alpha}\right) e^{-\alpha a}\right)$$

The temperature gradients generated within each bandwidth superpose if k and α are assumed nonvarying. This simplifying assumption was made; it is valid in the temperatures of interest - below 1100°C.

The multiple curve graph of Figure 18 brings together several important distributions if one is to perform a spectral integration of window absorption heat loads. The distributions were appropriately convoluted to provide weighting of the flux being absorbed in each spectral interval. Spectral transmissibility of the window is shown in Figure 19.

The blackbody distribution induces severe heating as energy is present in the transition bands of the window. The sea-level solar spectrum is considerably more benign with little energy in the dangerous transition bands.

The results of these calculations are given in Tables 7 and 8 below and are shown graphically in Figures 20 and 21.

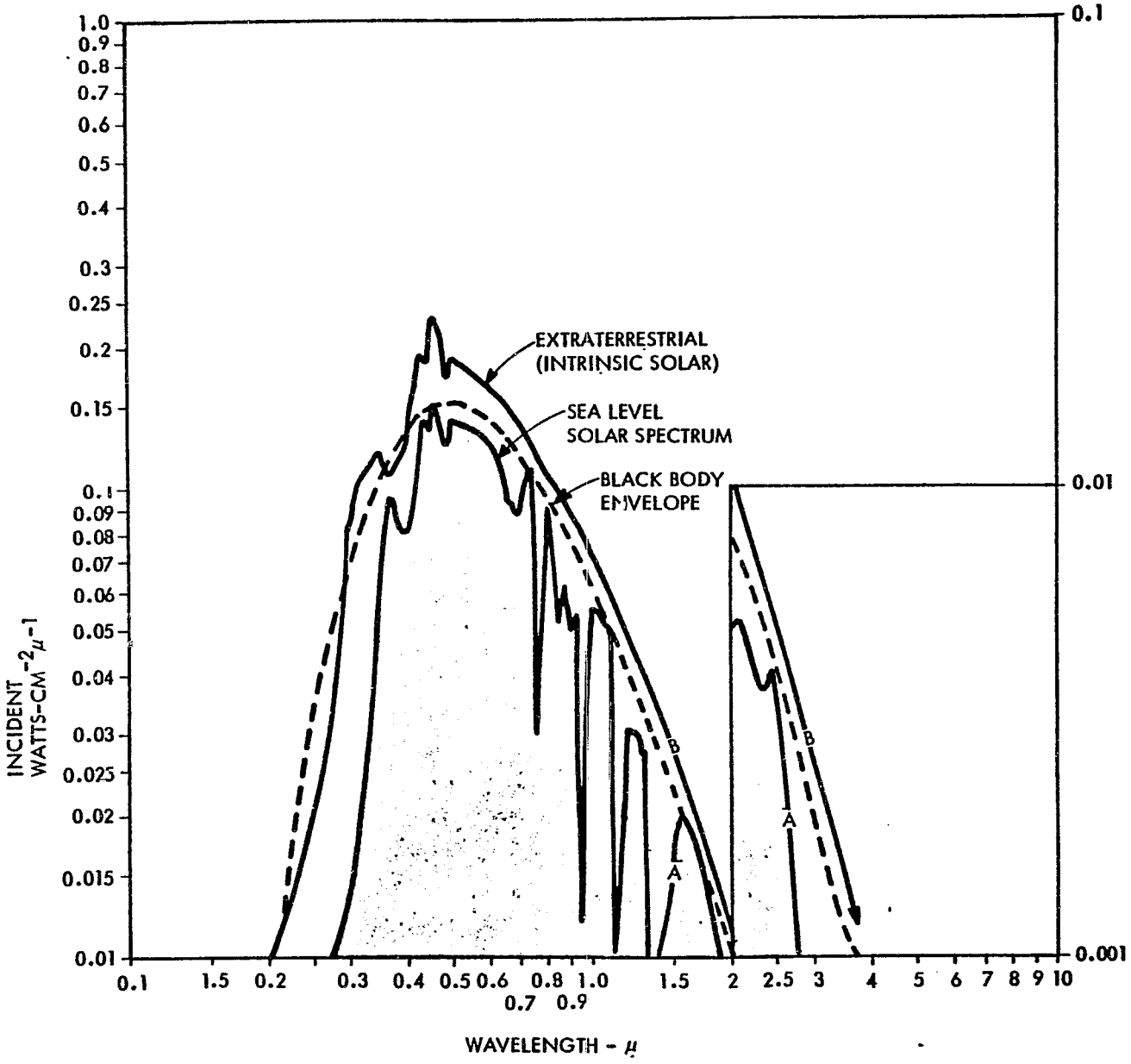

Figure 18. Spectral Energy Distribution

TABLE 7

SPECTRAL INTEGRATION OF BLACK BODY FLUX ABSORPTION
BY A
GE TYPE 125 QUARTZ WINDOW

λ μ	Fomax $W\ cm^{-2}$	$f_{\Delta 2}$ %	$F_{\Delta 2}$ $W\ cm^{-2}$	$\bar{T}$ %	C $\ell n\ \bar{T}$	WINDOW THICKNESS (CM) & ΔT 1.0	2.0	3.0	4.0	5.0	6.0
.16-.18	1300	.045	.585	10.	2.30	12	17	18			
.18-.20	1300	1.0	1.3	25.	1.39	27	51	61	65	66	67
.20-.225		.33	4.29	55.	.598	62	172	274	353	410	447
.225-.24		.30	3.90	72.	.328	37	119	219	321	414	497
.24-.26		.52	6.76	78.	.248	51	173	333	509	685	853
.26-.275		.70	9.1	94.	.0619	19	74	160	273	410	568
.275-.300		1.3	16.9	97.	.0306	18	71	156	272	417	589
2.6-2.7		.25	3.2	85.	.162	17	60	121	194	275	358
2.7-2.9		.5	6.5	85.	.162	34	122	246	395	558	728
2.9-3.3		.6	7.8	88.	.128	33	120	250	409	589	782
3.3-3.5		.3	3.9	78.	.248	30	100	192	294	395	492
3.5-3.7		.2	2.6	58.	.545	35	101	166	218	258	285
3.7-3.8		.05	.65	35.	1.05	12	27	36	41	43	44
3.8-4.0		.05	.65	17.	1.77	14	23	25	26	26	26
4.0-4.3		.05	.65	4.	3.22	12	14	14	14	14	14
TOTAL RISE						413	1244	2271	3402	4578	5768

ORIGINAL PAGE IS
OF POOR QUALITY

TABLE 8

SPECTRAL INTEGRATION OF SOLAR FLUX ABSORPTION

BY A

GE TYPE 125 QUARTZ WINDOW

μ / λ	W-cm^{-2} Fomax	% $f_{\Delta\lambda}$	W cm^{-2} $F_{\Delta\lambda}$	% T	ℓn T C	WINDOW THICKNESS & ΔT TEMPERATURE RISE ^{o}K 1.0cm	2.0cm	3.0cm	4.0cm	5.0cm	6.0cm
.16-.18	1300	.010	.130	10	2.30	3	4	4	4	4	4
.18-.20	1300	.020	.260	25	1.39	5	10	12	13	13	13
.20-.225	1300	.066	.858	55	.598	12	34	55	71	82	89
.225-.24	1300	.060	.780	72	.328	7	24	44	64	83	99
.24-.26	1300	.086	1.12	78	.248	8	29	55	84	113	141
.26-.275	1300	.178	1.31	94	.0619	5	19	41	70	104	144
.275-.300	1300	.650	8.45	97	.0306	9	35	78	136	209	294
2.6-2.7	1300	.012	.156	85	.162	1	3	6	9	13	17
2.7-2.9	1300	.025	.325	85	.162	2	6	12	20	28	36
2.9-.3.3	1300	.020	.260	88	.128	1	4	8	14	20	26
3.3-3.5	1300	.01	.130	78	.248	1	3	6	10	13	16
3.5-3.7	1300	.006	.078	58	.545	1	3	5	7	8	9
3.7-3.8	1300	.002	.026	35	1.05	.4	1	1	2	2	2
3.8-4.0	1300	.002	.026	17	1.77	.5	1	1	1	1	1
4.0-4.3	1300	.002	.026	4	3.22	.5	.5	1	1	1	1
TOTAL RISE						56	176	329	506	694	892

ORIGINAL PAGE IS
OF POOR QUALITY

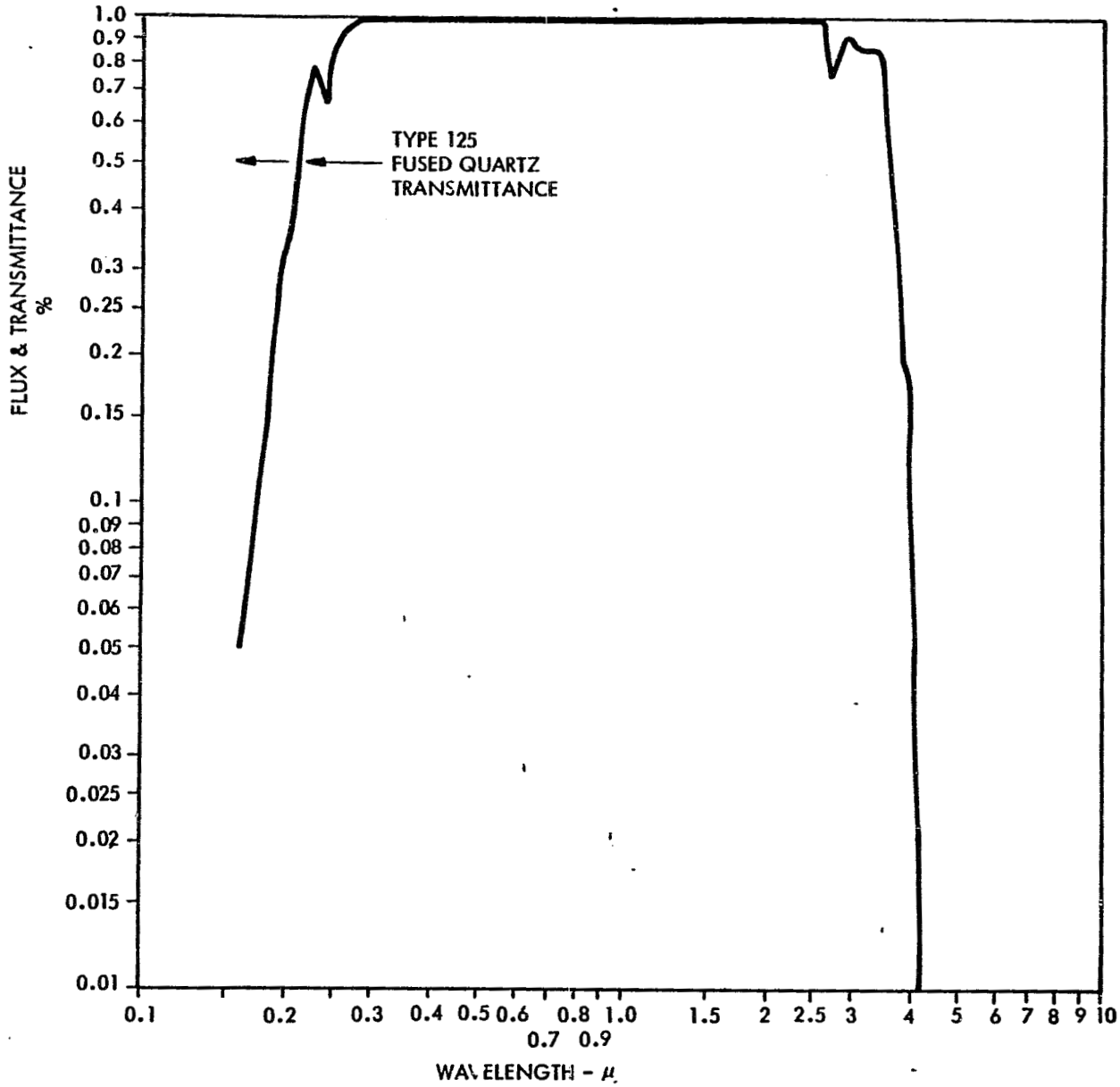
TYPE 125
FUSED QUARTZ
TRANSMITTANCE
FLUX & TRANSMITTANCE
%
1.0
0.9
0.8
0.7
0.6
0.5
0.4
0.3
0.25
0.2
0.15
0.1
0.09
0.08
0.07
0.06
0.05
0.04
0.03
0.025
0.02
0.015
0.01
0.1
0.2
0.3
0.4
0.5
0.6
0.7
0.8
0.9
1.0
1.5
2
2.5
3
4
5
6
7
8
9
10
WAVELENGTH - μ

Figure 19.

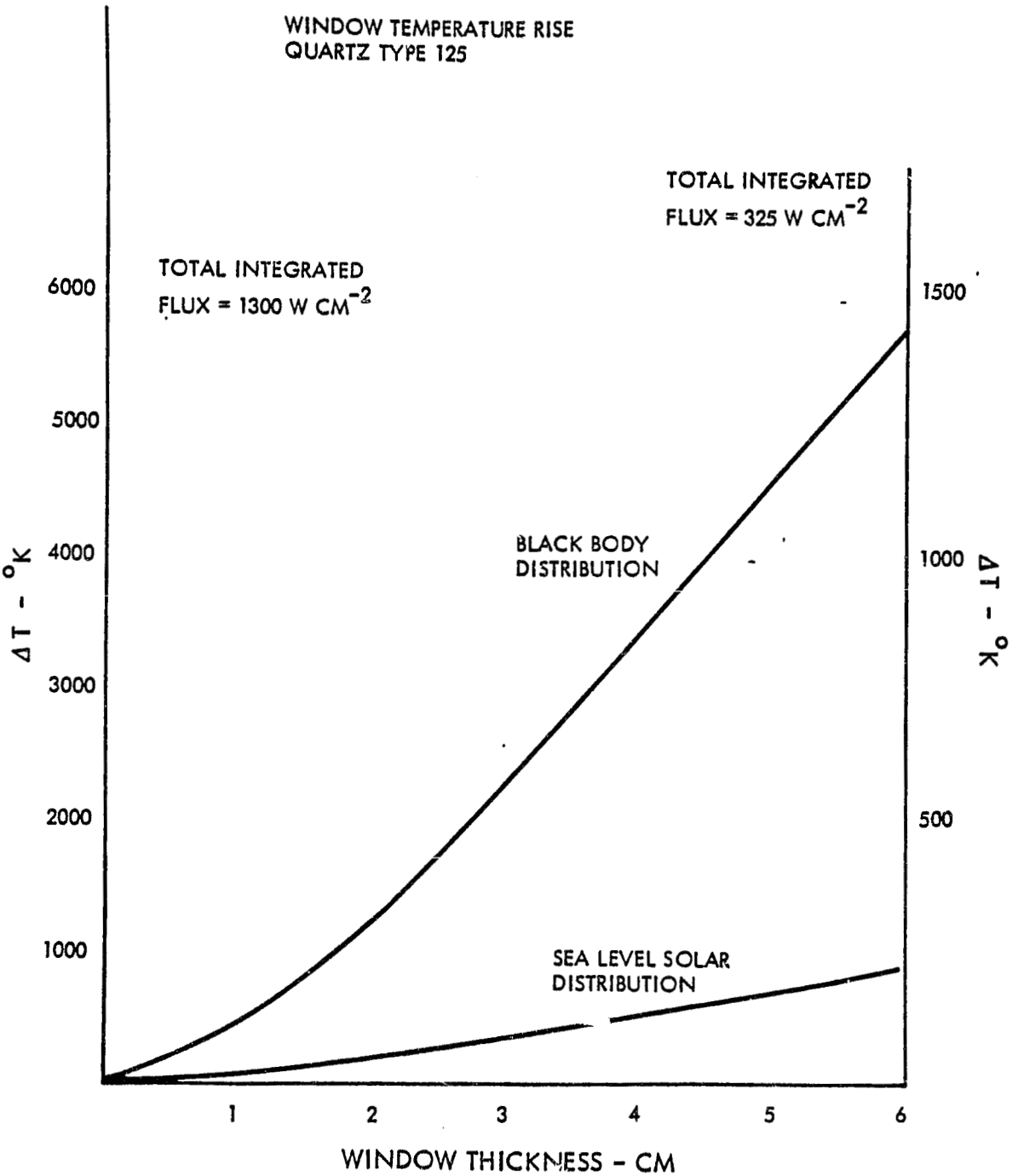

Figure 20. Window Temperature Rise Quartz Type 125 versus Window Thickness

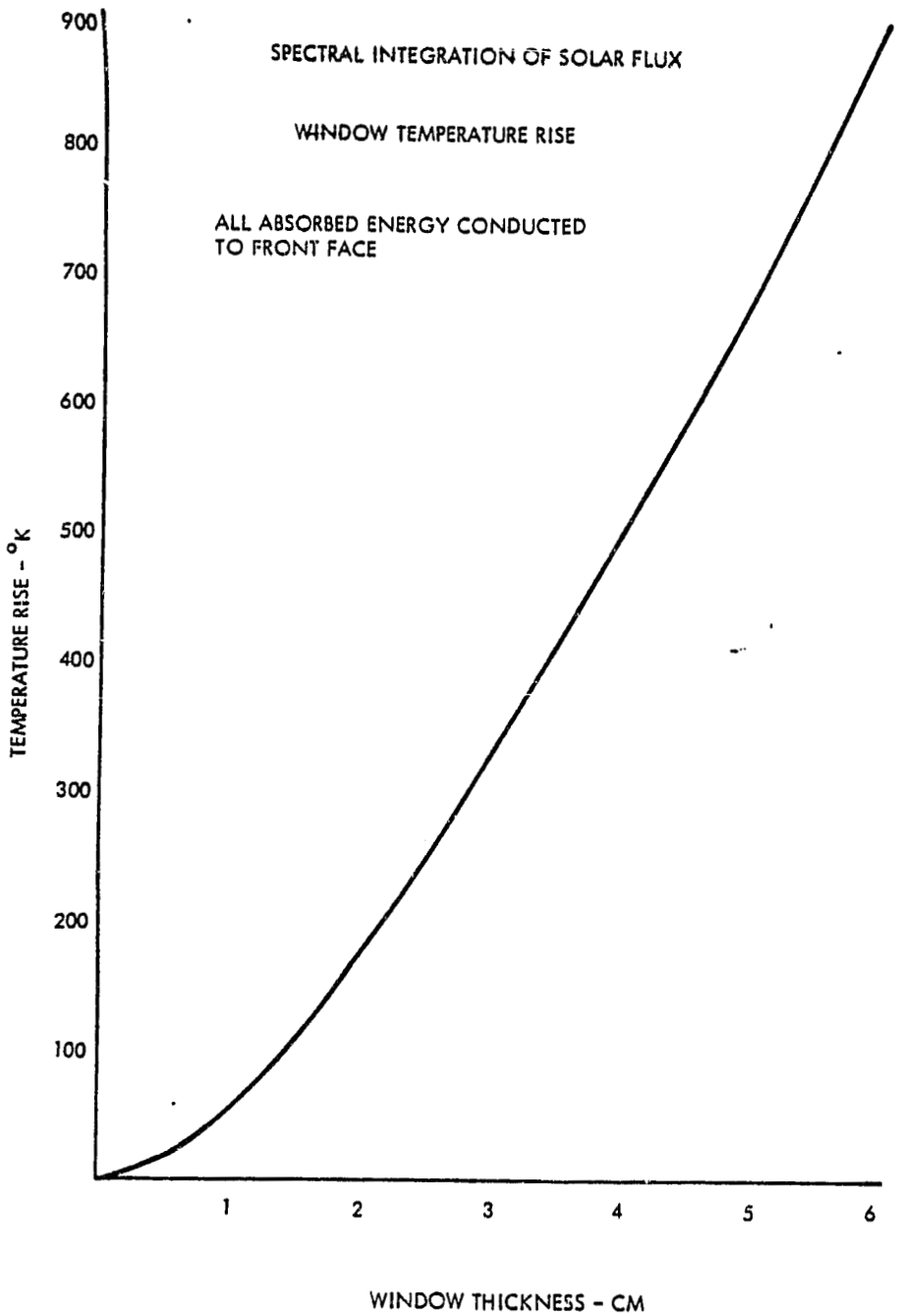

Figure 21. Window Temperature Rise versus Window Thickness

WINDOW SIZE LIMITS

Inasmuch as the window temperatures have been shown to rise dramatically with increasing thickness, the question of window scalability must be addressed.

Investigation shows that the window is well within its safety limits over the entire range of pressures and power levels specified by the contract.

Figure 22 is a window thickness calculation nomogram, and it shows the window is capable of safe operation throughout the entire power pressure envelope. Possible problems could arise if receiver inlet air temperature rises above 1800°F but this has been shown in the Brayton cycle conditions to be generally unlikely; this limit would be exceeded with a recuperator effectiveness of $\xi = 0.9$ when turbine inlet temperature exceeds 2600°F in a pressure ratio 4 machine, see Figure 8.

The Window Limit Safety Nomogram, Figure 22, provides a rapid means for calculating the required window thickness as a function of receiver power and pressure ratio. The required diameter may then be compared to window thickness temperature limit which is shown in the upper left hand corner of the figure. The graph is based on the following assumptions:

a. The window is a circular quartz disk clamped at the edges.

b. Window stress is limited to 1000 psi bending.

c. Spectral absorption and heating is as calculated in the preceeding section.

d. The window is located at the exit aperture of the compound parabolic concentrator described earlier.

ORIGINAL PAGE IS
OF POOR QUALITY

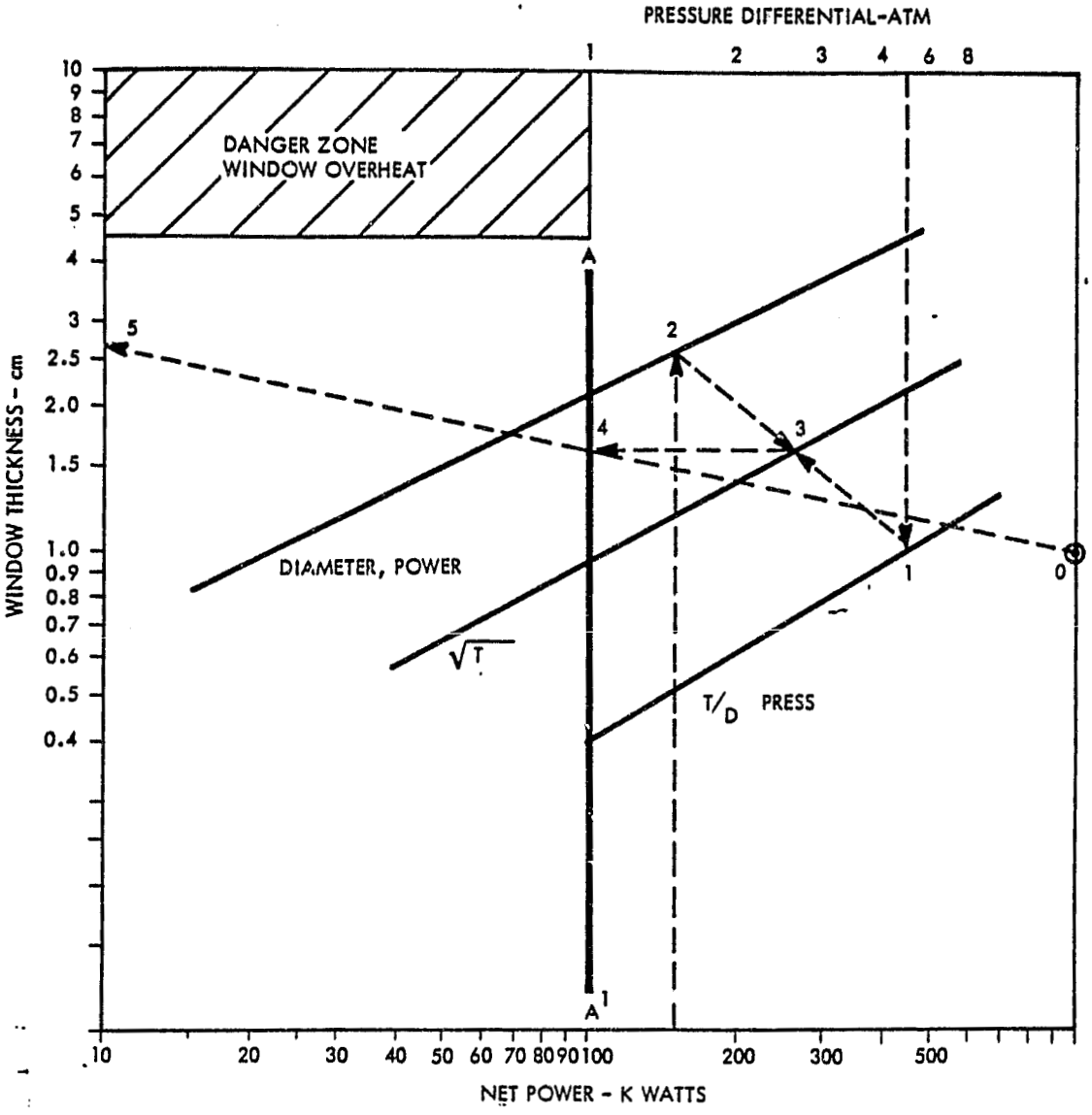

Figure 22. Window Limit Safety Nomogram

INSTRUCTIONS FOR NOMOGRAM USE

1. Enter the graph at the appropriate pressure differential on the upper abscissa scale. (Example: 5 ATM)

2. Proceed vertically downward to the T/D, Press line. (Example: Point 1)

3. Enter the graph at the appropriate power on the lower abscissa scale. (Example: 150 kw)

4. Proceed vertically upward to the DIPMETER, Power line. (Example: Point 2)

5. Draw a line between the intersection points and find the intersection on the $\sqrt{T}$ line. (Example: Point 3)

6. Proceed horizontally from the intersection on the $\sqrt{T}$ line to the vertical line A-A'. (Example: Point 4)

7. Now project a line from the bulls eye, Point O, through the intersection on line A-A' to the left most ordinate scale. (Example: Point 5)

8. Finally, read the window thickness on the left ordinate scale and assure it is below the danger zone.

NOTE: The example given here describes a receiver suitable for use with a pressure ratio 6 Brayton engine at 150 kw thermal input. Shaft power out would be approximately 70 kilowatts (95 HP).

MATERIAL SELECTION

The designed operating parameters of the HTSTR, including temperatures ranging from 2000° to 3000°F and the possibility of reactive atmospheres, requires the use of high refractory ceramic materials as heat exchanger components. The most likely candidates include silicon-carbide for tube and extended surface receivers; and cordierite, mullite and silicon-carbide for the matrix receivers. The generalized properties of these materials include high temperature stability in oxidizing and chemically active atmospheres, thermal shock resistance, capability of fabricating general shapes and scaling in size, and relative feasibility of material cost and availability.

Material Properties

Candidate materials can be classified into three groupings: carbides and nitrides; refractory oxides; and fiber ceramics. The strong covalent bond displayed by the carbides and nitrides, result in very high melting points, and generally high temperature corrosion and erosion resistance. Both SiC and Si_3N_4 are employed in high temperature applications, and are candidates for advanced turbine components. SiC, exhibiting the highest operating temperatures, has been fabricated into tubes employed successfully as heat exchanger components in solar receiver designs. The high thermal conductivity and emissivity of SiC makes this material an excellent heat exchanger candidate. The state-of-the-art fabrication techniques makes available a high density, impermeable, SiC body suitable for pressurized systems.

The refractory oxides, consisting of high alumina bodies, have been employed in the traditional high temperature application of furnace components and insulators. Cordierite exhibits the highest thermal shock resistance of any ceramic material maximum temperature of operation for cordierite is 2200°F in air. High purity alumina may be used at temperatures as high as 3180°F, however, thermal shock resistance of dense

alumina may not be sufficient to withstand the thermal fluxes generated in a receiver. Mullite is a third alumino-silicate which shows promise as a receiver material.

The third group of materials, fiberous ceramics, are of interest due to their extrinsic nature, a result of fabrication, rather than intrinsic properties of the crystal lattice. Typically, these materials exhibit excellent thermal shock resistance, high thermal resistivity, and low density. Material degradation will usually begin however above $2000^{o}F$. A relatively new product from 3M, Nextel 312, consisting of $3Al_2O_3 \cdot BO_2 \cdot 2SiO_2$ will retain its properties at extended service to $2600^{o}F$. Nextel 312 is relevant for gasket and sealing materials and may be interesting in a matrix configuration of multiple layers of woven strand.

Silicon Carbide

The materials selected for the early absorber matrices capitalized on the IRCM technology since it had gone through several improvement steps. The materials used in the test at White Sands were both the low density sintered SiC and the reaction sintered SiC, with most of the testing done with the latter. No changes were observed in either material as a result of the test.

The material used in Sanders' 1/4 MWt receiver experiment was made by taking the low density SiC material and impregnating it with more Sic by infiltrating an organic resin into the pores, converting it to carbon by pyrolysis, and then infiltrating with elemental silicon. The carbon and silicon react readily to form SiC, nearly filling the pores. The resulting material had greatly improved physical properties, especially thermal conductivity and strength. Testing performed to date on the system has shown no degradation of the Sic

An alternative method of fabricating matrices of dense SiC employs the technique of mixing fine powders of α-SiC graphite, mixed with a plasticizer, and formed into shape by the appropriate methods. This process employs a siliconizing step following the removal of organics. The concentration of free silicon in the body can be controlled with an 8% level as the lower limit.

Cordierite

Two sets of absorber matrix panels were made from cordierite because of its low cost and advanced fabrication techniques. One was made by corrugation, with layers alternating between corrugated sheets and flat sheets, similar to a thick piece of corrugated paper.

The other set was made by an embossing approach. A calendered sheet of plasticized ceramic powder is passed through an embossing machine that has one smooth roller and grooves in the other roller, and with the grooves running parallel to the axis of rotation. By adjusting the inner-roller spacing, ribs will be generated on the material by squeezing some material into the roller grooves. These ribs form stand-offs when a sheet of the material is wrapped in a spiral, thereby generating the cells. The cell geometry can be square, rectangular, triangular or other shape.

Cordierite is most economically made from natural minerals such as kaolin, talk, kyanite, silica and bauxite. The nominal composition of the various materials is tabulated below. Since the price of the raw materials vary widely, it is necessary to perform an economic study as part of the selection process involving pricing, purity, and preparation required.

CORDIERITE - $2\,MgO \cdot 2A\ell_2O_3 \cdot 5SiO_2$

KAOLINITE - $A\ell_2O_3 \cdot 2Sio_2 \cdot 2H_2O$

TABLE 9

MATERIAL	MAXIMUM TEMP (^{o}F)	ATMOSPHERE	THERMAL EXPANSION $x10^{-7}/^{o}C$	THERMAL CONDUCTIVITY @1000^{o}C (W/cm^{o}K)	THERMAL SHOCK RESISTANCE
SiC	2700	Air	50	0.3	Good-Fair
	2950	N_2,He			
Si_3N_4	2220	Air	40	0.06	Fair
	2750	N_2,He			
BN	2220	Air	68	0.2	Fair
	3000	N_2			
	2900	H_e			
Al_2O_3	3180	Air	85	0.08	Poor
(99.9)	3025	N_2,He			
Cordierite	2200	Air	25	0.02	Excellent
	2025	N_2,He			
Mullite	2900	Air	50	0.03	Fair-Poor
	2700	He,N_2			
Fiber (Nextel 312)	2500	Air, N_2,He			Excellent

TALC	-	$3MgO \cdot 4SiO_2 \cdot H_2O$
SILICA	-	SiO_2
BAUXITE	-	$Al_2O_3 \cdot 3H_2O$
KYANITE	-	$Al_2O_3 \cdot SiO_2$

The materials must be calcined to remove the chemically bonded water if present. After calcining, they are mixed using a ball mill, or other device, which breaks down the particle size and provides a uniform, intimate mixture. The necessary organic binders are added part way through this process, and thereby distributed. These additives provide both the initial strength and some lubrication between grains of the ceramic powder during the forming process. Various waxy, long chain polymers are used for this purpose, sometimes in conjunction with a liquid. The additive system we will refer to here uses polyethylene and an oil, avoiding the shrinkage and cracking that sometimes occurs with aqueous systems. The presence of polyethylene means the mixture must be heated to accomplish forming.

The mixture is densified and de-aired by extrusion through a flat orifice. This step is needed to eliminate voids and promote good inter-particle contact necessary for the final step of sintering. The material is now in the form of a flat sheet, ready for the calendaring/embossing step.

Matrix Receiver

Matrix configurations composed of silicon-carbide and cordierite bodies have been fabricated up to 28 inches in diameter.

Table 10 relates the applicability of various forming techniques to rates of production. Extrusion probably is suitable for the highest production rates though the process has the highest tooling costs.

TABLE 10. APPLICABLE FORMING TECHNIQUES

TECHNIQUE	APPROACH	PRODUCTION RATE
LAYED-UP	STACKING OF INDIVIDUAL SHAPES TO FORM ASSEMBLY.	LOW
CORRUGATED	ALTERNATING CORRUGATED AND UNCORRUGATED LAYERS, PLACED FLAT OR FOLLED UP.	MODERATE
EXTRUDED	PUSHING PLASTICIZED CERAMIC POWDER THROUGH DIE TO FORM SHAPE.	HIGH
CALENDARING	PLASTICIZED CERAMIC POWDER IS PASSED BETWEEN ROLLERS TO FORM A SHEET AND IS THEN WOUND AROUND A MANDREL TO FORM A DISK.	HIGH
EMBOSSING	CALENDARED SHEET IS PASSED THROUGH ROLLERS, ONE OF WHICH HAS GROOVES TO FORM RIBS ON SHEET.	HIGH

Ultimate design flexibility in terms of maximum holes per square inch for matrix receivers is less with extrusion than with calendering. Extrusion dies may be practical to 400 holes per square inch. Calendering, in contrast can now be accomplished with 1200 holes per square inch and may be practical at 1600 holes per square inch. Extrusion processes tend to favor an intermediate solid fraction (25-60%) while calendering is almost completely flexible in this respect (25-80%).

The extrusion process is well suited to thick (axially extended) pieces less than 18 inches in diameter. Calendering is useful for thinner (length <4.0 inches) pieces, but the part diameter is currently limited by firing constraints about 40 inches or less.

Tube and Extended Surface Receivers

The material requirements for tube and extended wall receivers are more stringent than the matrix receiver. The complexity of the unit design increases, including considerations of large pressure drops across thin walls, sealing at the ends of components, and fabricating complex shapes. Sintered SiC is the prime candidate for such systems.

SiC tubes and other complex shapes are formed through extrusion, mold injection, hot pressing, and slip casting techniques. Norton has formed SiC tubes 5 to 6 inches in diameter to about 7 feet in length by slip casting. This technique forms a uniform body as evident by performance. Tubes 1 inch OD with a 1/4 inch wall were pressurized internally to 500 psi with He gas exchange media with very little leakage.

The bond connecting two sections of preformed ceramic or sealing the ends typically has been the weak point of the system. Bonding techniques (Table 11) are generally required in tube and extended surface receivers. Bonding does occur in lay-up and rolled-up (calendered) matrix fabrication, but it is a parent material process intrinsic in the firing of the matrix. The discrete post-firing bonding processes

TABLE 11. BONDING TECHNIQUES FOR CERAMICS

TECHNIQUE	APPROACH	ATTRIBUTES
SILICATE	SILICA CONTAINING LIQUID MATERIAL; e.g., SODIUM SILICATE, IS APPLIED, OFTEN MIXED WITH POWER	LOW COST, LIMITED BY GLASSY PHASE. LOW STRENGTH BEFORE FIRING
PHOSPHATE	PHOSPHORIC ACID MIXED WITH SOLIDS.	SOME STRENGTH BEFORE FIRING.
PRESSURE	POWDER OR OTHER ACTIVE MATERIAL PLACED ON SURFACES TO BE BONDED. ASSEMBLY IS HEATED UNDER LOAD TO FORM BOND.	CAN BE DONE TO ATTAIN 100% JOINT STRENGTH. REQUIRES CAREFUL FIXTURING.
REACTION	FOR BONDING SILICON CARBIDE, FOR EXAMPLE, SILICON AND CARBON ARE PLACED ON SURFACES TO BE BONDED AND THE JOINT IS HEATED.	CAN ATTAIN 100% JOINT STRENGTH. NOT APPLICABLE TO OXIDE CERAMICS IN GENERAL.
BRAZING	CERAMIC IS ATTACKED BY PROCESSING, GENERATING THIN METAL LAYER, THEN NORMAL BRAZE.	LIMITED BY METAL AT HIGH TEMPERATURE. GOOD FOR HERMETIC JOINTS.

shown in the table add to the fabrication costs of tubed and extended surface receivers. Except in the case of pressure sintering and reaction bonding, the fired joints represent material discontinuities and are therefore subject to thermal stress failures and their own temperature limitations.

The maximum service temperature of tubed and extended surface receivers has been limited by bond joint properties to less than 1100°C (2000°F). Developmental work has extended this limitation into the range of temperatures relevant to the bulk lattice.

Although this bonding development has been done on a small scale, it has demonstrated bonded joints of quality equivalent to the bulk material.

Availability and Cost

The selection of the receiver will be influenced by availability and cost of materials for constructing the absorber. Each material will not be applicable to the several configurations because of process technology and material properties.

Potential forming methods for the three types of receivers are listed in Table 12, along with comments on cost. One aspect that significantly affects cost is dimensional requirements (which is not shown). If the tolerances are large, it is possible to do any necessary machining before firing at low cost, while close tolerances will require machining in the fired state when machining is much slower. Experience suggests that tolerance requirements will be lowest for the matrix receiver and most demanding for the extended surface receiver.

The various materials are ranked in Table 13 by cost of raw material and cost of processing. Materials with high costs of raw material and processing tend to be much less attractive because of these factors.

TABLE 12. POTENTIAL FORMING METHODS

RECEIVER TYPE	FORMING METHOD	TOOLING COST	PRODUCTION COST	OTHER ATTRIBUTES
MATRIX	EMBOSSING	MODERATE	LOW	MODERATE CROSS SECTION
	CORRUGATING	LOW	LOW-MODERATE	LARGE CROSS SECTION
	EXTRUSION	HIGH	LOW	LIMITED CROSS SECTION
TUBE	EXTRUSION	HIGH	LOW	LONG LENGTHS
	ISOSTATIC PRESSING	LOW	LOW-MODERATE	LIMITED LENGTH
EXTENDED SURFACE	SLIPCASTING DIE	LOW	MODERATE-HIGH	COMPLEX SHAPES
	PRESSING	LOW	LOW	SIMPLE SHAPES
	MOLDING	MODERATE	LOW-MODERATE	INTRICATE SHAPES
	HOT PRESSING	MODERATE	HIGH	MOST MATERIALS SIMPLE SHAPES

TABLE 13. MATERIALS COST

	RAW MATERIAL	PROCESSING
LOWEST COST	CORDIERITE	CORDIERITE
	MULLITE	MULLITE
	ALUMINA	ZIRCONIA
	ZIRCONIA	ALUMINA
	SILICON CARBIDE	
	REFRACTORY METALS	
	OTHER CARBIDES	
HIGHEST COST	NITRIDES	SILICON CARBIDE
		REFRACTORY METALS
		NITRIDES
		OTHER CARBIDES

THERMAL STRESSES

The thermal stresses imposed on a flat restrained finite segment of candidate ceramic materials is calculated below.

These calculated values differ significantly from the stresses likely in heat transfer tube walls or in the extended surface monolith (finned bell jar). Stresses in real hardware can be alleviated by flexure and distortion; but stress concentrations near discontinuities in a three-dimensional object with compound curvature can seriously aggrevate the maximum stress levels.

$$q = \frac{kA}{\ell} \Delta T \qquad \text{conduction} \qquad (1)$$

$$F = \frac{q}{A} = \frac{k}{\ell} \Delta T \qquad \left(F = \text{flux} = \frac{\text{heat flow}}{\text{area}}\right)$$

$$\frac{d\ell}{\ell} = \alpha \Delta T \qquad \text{expansion} \qquad (2)$$

$$\frac{d\ell}{\ell} = \frac{\sigma}{E} \qquad \text{stress/strain} \qquad (3)$$

Rearranging (1)

$$\frac{F}{k} = \frac{dT}{d\ell}$$

Combining (2) and (3)

$$\alpha \Delta T = \frac{\sigma}{E}$$

$$\sigma = \alpha \Delta T E \qquad (4)$$

Combining (1) and (4)

$$\frac{F\ell}{k} = \frac{\sigma}{\alpha E}$$

$$\sigma = \frac{F\ell\alpha E}{k} \qquad (5)$$

In expression (5) σ represents the difference in stress levels across a full thickness, ℓ. If the assumption is made that a neutral axis exists at the mid-wall plane, then ℓ may be taken as 1/2 wall thickness and σ then represents the absolute value of the tensile (and compression stress levels at the wall surface(s).

Key thermal stress properties of candidate materials are given in the table below:

	$A_{1_2}O_3$	Sic	Cordierite	BN	Mullite	Units
α	20.E-7	50.E-7	17.E-7	68.E-7	50.E-7	lb/in^{-2}
k	1.4	1.4	0.2	1.0	1.14	$\frac{BTU}{in.hr.^oF}$
E	40.E-7	55.E-7	7.E-6	1.5E-7	22.E-6	lb/in^{-2}

The results of evaluating equation (5) to determine nominal stress values in the candidate materials is shown below.

Flux $\frac{BTU}{in^2.hr.^oF}$ (W/cm^2)	$A_{1_2}O_3$	SiC	Cordierite	BN	Mullite
			Stress - lb/in^{-2}		
2000 (100)	7860	27000	8180	1400	110000
1000 (50)	3930	13500	4090	701	55200
440 (20)	1570	5400	1640	280	22100
220 (10)	786	2700	818	140	11000
110 (5)	393	1350	409	70	5520
44 (2)	157	540	164	28	2210

These values are calculated over the range of flux values (2 - 100 watts/cm^{-2}) likely to be encountered in the HTSTR for a typical wall thickness of 0.125 inches (half wall = 0.063 inches).

The results show that alumina, silicon carbide, and cordierite are viable candidate materials for use in the tubed and open aperture extended surface receivers which require through wall conduction of heat from an absorbing surface to a convecting surface. These materials exhibit operating stresses sufficiently below the modulus of rupture to hold crack tip growth rates to acceptably low rates. Boron nitride with its low MOR and mullite with very high stresses would not represent wise material choices for this application and concept.

Based on our own operating experience at Sanders over the past three years, silicon carbide and cordierite are known to be well suited to application in matrix or windowed extended surface receivers where thermal diffusivity and expansion are the controlling parameters. In these concepts radiant is absorbed on the surface of a thin ceramic section and is then convected off the same surface. Thermal stresses in these applications are (based on modeling performed under prior contracts) approximately an order of magnitude smaller.

Mullite is known to be a well suited sensible heat storage media and has been used in the steel industry (blast furnaces) for decades. It exhibits long life in those applications. Mullite could be used in the matrix receiver as the auxiliary thermal buffer mass where it would be isolated from radiantly and convectively induced thermal shocks.

WEIGHT ESTIMATE

The four configurations with options were anayzed to provide a weight and center of gravity estimate. Figures presented below refer to the 70 kw baseline design.

Configuration	Storage	Weight	CG
Matrix, Windowed	No	180	12.7
Matrix, Windowed	Yes	306	14.1
Extended Surface, Open	No	131	15.8
Extended Surface, Windowed	Yes	337	13.9
Tubed	Yes	287	15.2

REGIMES OF OPERATION

The regimes of operation of the investigated concepts are shown on Figure 23. The windowed matrix and windowed extended surface receivers are compatible with the entire range of interest. The only cautionary note is the requirement to keep inlet air to the receiver at 1800°F or below.

The extended surface receiver runs into temperature limitations at lower output air temperatures due to the through wall temperature gradient. At increased power levels the limitations are induced by axial temperature gradients along the bell jar. Maximum pressure levels are limited by the ability of the convoluted jar to withstand external pressure.

The tubed receiver also experiences a high temperature limit because the heat must be conducted through the tube walls to the working fluid. Maximum power levels are limited by the hoop stress imposed on the tubes by radial heat flow. The tubed receiver is fully compatible with the specified pressures

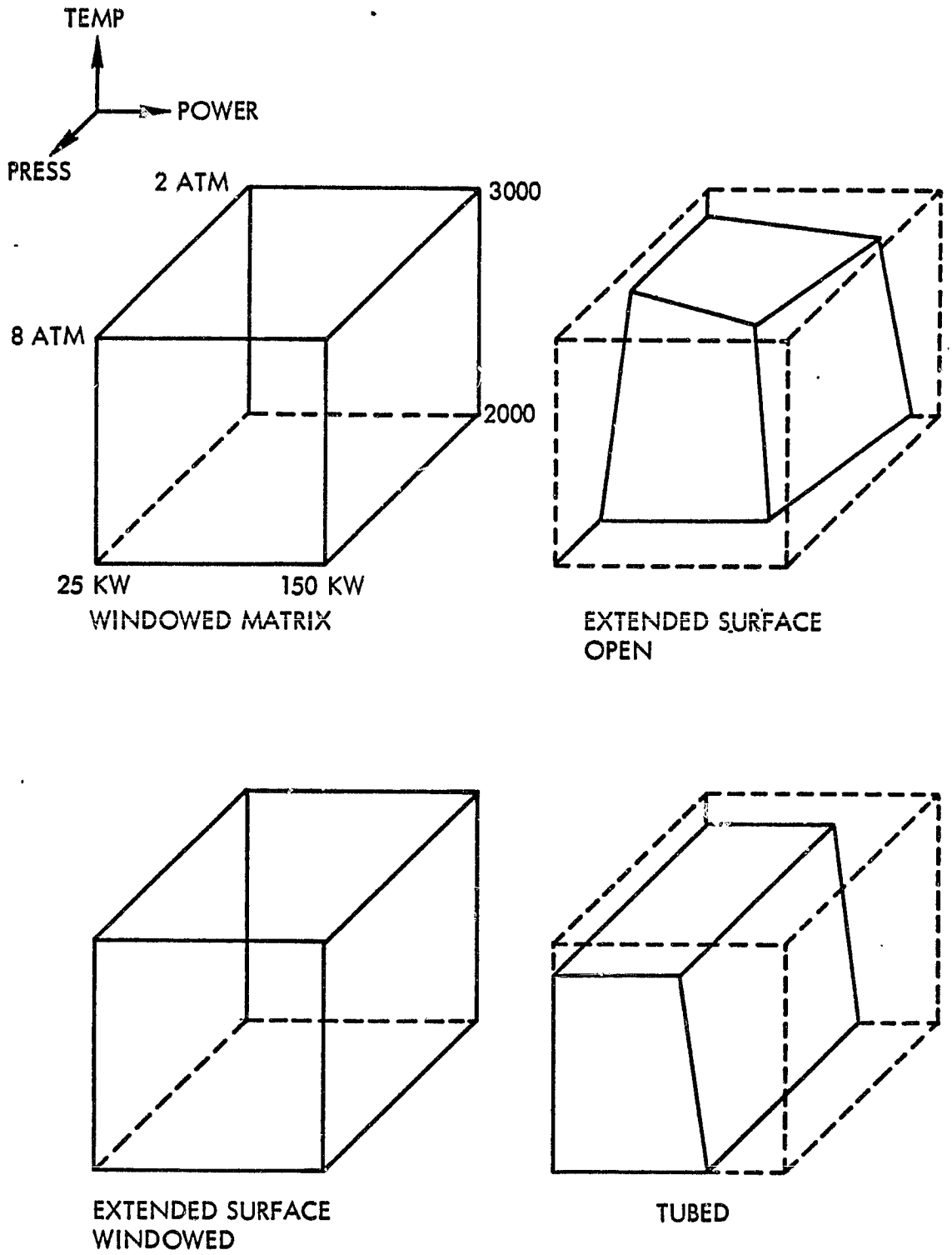

Figure 23. Receiver Regimes of Operation

RECOMMENDATIONS

The windowed receivers are recommended for their superior capabilities. The two windowed concepts are very comparable in their overall evaluation but the balance favors the matrix receiver for the reasons given below.

The matrix receiver panels are fully within present day production capabilties.

Thermal buffer material can be optionally installed or omitted.

Thermal buffer material can be a less expensive material (Mullite, Alumina) than the matrix (silicon carbide) because it is not exposed to step transients.

Radiation losses from the thermal buffer are trapped by the matrix and are returned to the airstream; the energy cannot escape through the aperture.